RESEARCH ARTICLE SUMMARY

BIOPHYSICS

Measurements of molecular size and shape on a chip

Xin Zhu†, Timothy J. D. Bennett†, Konstantin C. Zouboulis, Dimitrios Soulias, Michal Grzybek, Justin L. P. Benesch, Afaf H. El-Sagheer, Ünal Coskun, Madhavi Krishnan*

Full article and list of author affiliations: https://doi.org/10.1126/science.adt5827

INTRODUCTION: The pursuit of experimental methods for high-resolution characterization of biomolecular properties continues to drive innovation in analytical technology development. Size and shape in particular are critical stereometric discriminators between molecular species and states in solution. We describe a microchip-based method that leverages the combined advantages of random thermal motion and size-dependent confinement effects at the nanoscale to achieve high measurement sensitivity to molecular conformation under native conditions in the solution phase.

RATIONALE: This approach visualizes the motion of fluorescently labeled molecules within fluid-filled slits using widefield microscopy. Shallow slits constrain molecular movement vertically, whereas periodic indentations act as entropic traps, increasing the time molecules spend in deeper regions. This effect is size-dependent: Larger molecules remain trapped longer. By engineering the number of accessible states—translational, configurational, and conformational—entropy can be harnessed at the nanoscale to amplify the influence of molecular size and shape on escape times. Precise measurement of these escape times furnishes insight into both the hydrodynamic radius and the diameter of the smallest bounding sphere enclosing the molecule, establishing a crucial link between solution-phase three-dimensional (3D) conformations and molecular models.

RESULTS: The technique offers a broad, customizable dynamic range for molecular weight measurements, spanning from 500 Da to at least 500 kDa. It can distinguish differences as small as two carbon atoms in small molecules and process complex samples. The single-molecule detection fosters exceptional sensitivity, currently detecting molecular concentrations as low as 10 fM. The method's speed and precision support quantification of intermolecular interaction strengths across more than six orders of magnitude in affinity constant and enable real-time monitoring of reaction kinetics. By tracking individual molecules, the approach also resolves molecular-state heterogeneity at the highest resolution. Lastly, we demonstrate the diagnostic potential of the technique by leveraging ligand-induced conformational changes in the insulin receptor to sense insulin levels in serum.

CONCLUSION: Escape-time stereometry (ETs) delivers (i) quantitative insight into molecular 3D structure, (ii) thermodynamic and kinetic data on interactions, and (iii) a high-speed, high-sensitivity detection platform for diagnostics, addressing a long-standing integration challenge in molecular measurement technology. ETs is likely to be particularly effective for detecting multimeric complexes formed through weak interactions, which are often difficult to identify with other methods. By enabling high-throughput, solution-phase conformation mapping to molecular models, ETs could support machine learning approaches for 3D structure prediction, validation, and inference. This capability is particularly valuable for studying complex structural problems, such as disordered proteins and RNA, and for detecting and characterizing rare molecular states. □

*Corresponding author. Email: madhavi.krishnan@chem.ox.ac.uk †These authors contributed equally to this work. Cite this article as X. Zhu *et al.*, *Science* **388**, eadt5827 (2025). DOI: 10.1126/science.adt5827

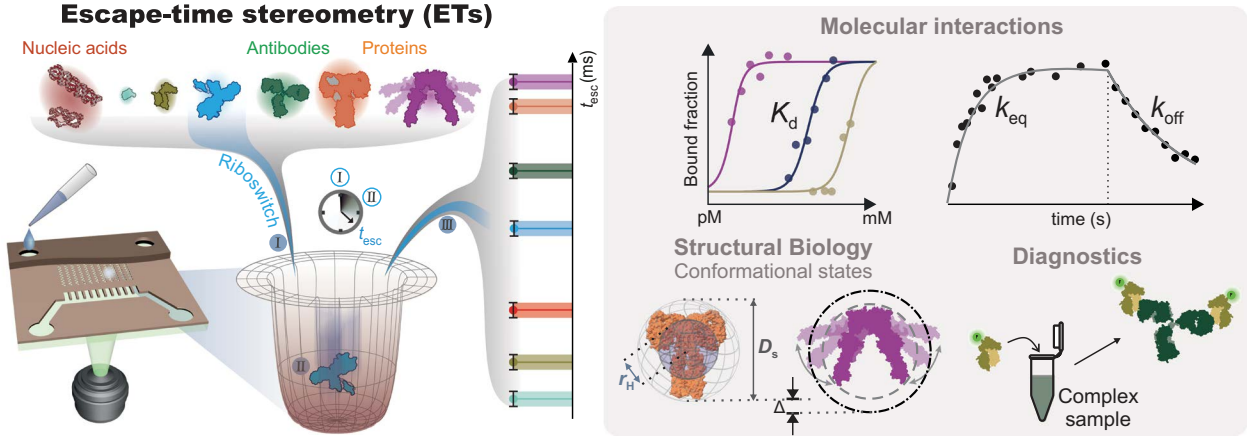

High-speed measurement of molecular size and shape in solution. Escape-time stereometry (ETs) leverages optical observation of single molecules diffusing through a nanoscale landscape of entropic traps. The average escape time (t_{esc}) from a trap serves as a precise indicator of a molecule's hydrodynamic radius (r_H) and bounding-sphere diameter (D_s), enabling a wide range of applications in molecular analytics and structure-conformation studies. K_d, dissociation constant; k_{off}, off-rate; k_{eq}, equilibrium constant.

BIOPHYSICS

Measurements of molecular size and shape on a chip

Xin Zhu[1]†, Timothy J. D. Bennett[1]†, Konstantin C. Zouboulis[1,2], Dimitrios Soulias[1], Michal Grzybek[3], Justin L. P. Benesch[1,2], Afaf H. El-Sagheer[4,5], Ünal Coskun[3,6,7,8], Madhavi Krishnan[1,2]*

Size and shape are critical discriminators between molecular species and states. We describe a microchip-based high-throughput imaging approach offering rapid and precise determination of molecular properties under native solution conditions. Our method detects differences in molecular weight across at least three orders of magnitude and down to two carbon atoms in small molecules. We quantify the strength of molecular interactions across more than six orders of magnitude in affinity constant and track reactions in real time. Highly parallel measurements on individual molecules serve to characterize sample-state heterogeneity at the highest resolution, offering predictive input to model three-dimensional structure. We further leverage the method's structural sensitivity for diagnostics, exploiting ligand-induced conformational changes in the insulin receptor to sense insulin concentration in serum at the subnanoliter and subzeptomole scale.

The pursuit of high-resolution biomolecular characterization has driven substantial advances in analytical technology development (*1*–*10*). However, most methods entail the use of strong electrical or optical fields, immobilization and/or tethering of molecules to surfaces, or the use of matrices. All these factors can perturb the integrity and function of biomolecules and their complexes, whose structure and conformation arise from the concerted action of weak inter- and intramolecular forces (*11*, *12*). Therefore, characterization methods in the solution phase that offer high-precision readouts while preserving molecular structure and properties remain highly sought after.

The friction associated with an object moving through a fluid carries a clear signature of its volume and shape and causes larger objects to travel a shorter distance on average in a given period of time. The Stokes' or hydrodynamic radius, r_H, quantifies this property and has been extensively used to characterize molecular species in solution (*13*–*16*). The shape of an object may be further captured in terms of its compactness given a fixed volume, as reflected in the diameter of the smallest sphere, D_s, enveloping it. This quantity shares similarities with the maximum spatial extent of the molecule, D_{max}, encountered in small-angle x-ray scattering (SAXS) (*17*) (Fig. 1C). Indeed, workhorse laboratory techniques such as size-exclusion chromatography exploit this molecular property to separate and sieve mixtures. Precise measurement of the size and shape of molecules—"molecular stereometry"—achieved by direct observation of molecular motion in a suitably tailored landscape thus offers the prospect of highly simplified structure-sensitive readouts traditionally believed to lie exclusively within the realm of high-resolution techniques (Fig. 1A) (*18*, *19*).

In this work, we leverage the combined advantages of random thermal motion and size-dependent confinement effects at the nanoscale to achieve high measurement sensitivity to molecular conformation under native conditions in the solution phase. Spatially constraining the vertical motion of an object diffusing in a geometrically tailored slit can dramatically enhance the time the object spends in local, deeper, "pocket" or trap regions, in a size-dependent fashion (Fig. 1, A and B, and movie S1). The larger the object, or the greater the degree of confinement in the parallel-plate slit region, the longer it resides in the trap. Engineering the number of states accessible to a molecule in the slit—e.g., translational, configurational, and conformational states—entropy in its various forms can be exploited at the nanoscale to amplify the impact of size and shape on molecular exit (escape) times. Low-power, widefield imaging of trapped molecules with a large-area camera detector confers on the method both speed and measurement precision (movie S1). The ability to tune the magnitude of the measured response with device geometry offers unprecedented sensitivity to molecular conformational properties, enabling the technique to outperform traditional solution-phase methods that rely solely on hydrodynamic friction, as will be demonstrated in this work (*16*, *20*, *21*). The technique offers wide and tailorable dynamic range in molecular weight readouts from 500 Da to at least 500 kDa, quantitative sensitivity to molecular concentration in solution, the ability to process complex samples, and readout reaction rates and equilibrium constants, all in a single platform, thus addressing a previously unmet integration challenge. We term the approach "escape-time stereometry" (ETs) and demonstrate the broad ramifications of the method's core working element, the "entropic fluidic trap," in a range of analytical application areas, including molecular diagnostics (*22*).

Spatial tailoring of translational entropy enables high-throughput measurements and molecular counting

In our experiments, we introduce fluorescent molecules at a concentration of 10 fM to 10 nM suspended in phosphate-buffered saline (PBS, ionic strength ~160 mM) into a series of parallel-plate slits of height h_1 that carry arrays of periodic cylindrical indentations of total height h_2 (Fig. 1, A and B). Similar to findings in previous work, the "pocket" nanostructures act as thermodynamic traps for single molecules in solution (Fig. 1B) (*3*, *18*, *19*, *23*). In contrast to previous work, the use of high salt concentrations renders charge-related electrostatic effects negligible, and the trap is expected to be effectively purely entropic (*22*, *24*) (supplementary text S1.4 and fig. S5). We image the diffusive dynamics of molecules, labeled on average with a single fluorophore, using standard widefield microscopy (Fig. 1A) (*3*). We measured average escape times, t_{esc}, for a variety of molecules from small organic fluorophores to disordered and globular proteins, nucleic acids, and protein complexes by imaging the chip for about 1 min in each case (Fig. 1, D and E, and Fig. 2A). Typical imaging conditions entail exposure times $t_{exp} = 5$ ms and an imaging rate of 100 Hz, unless stated otherwise (materials and methods). For low–copy number counting experiments (fig. S5 and supplementary text S1.3) and for experiments on the insulin receptor discussed later, slit surfaces were passivated by coating with polyethylene glycol to minimize nonspecific molecular adhesion (supplementary text S1.2).

For a small sphere whose radius $R \approx r_H \ll h_1$, we have $t_{esc} \propto r_H(h_2/h_1)$, which illustrates that the height modulation in the slit enhances molecular residence times by a factor h_2/h_1 compared with the free-diffusion value (Fig. 2C, red line; fig. S8; and supplementary text S3). This entropic enhancement of residence times in the pocket region is crucial to the method because it fosters high-throughput direct imaging of the escape process on the order of 100 to 1000 molecules in 1 min or less of measurement time, using both low incident optical power densities (~5 W/mm^2) and a large-area detector such as a camera chip. Our

[1]Physical and Theoretical Chemistry Laboratory, Department of Chemistry, University of Oxford, South Parks Road, Oxford, United Kingdom. [2]The Kavli Institute for Nanoscience Discovery, University of Oxford, Sherrington Road, Oxford, United Kingdom. [3]Center of Membrane Biochemistry and Lipid Research, University Hospital and Faculty of Medicine Carl Gustav Carus, Technical University Dresden, Dresden, Germany. [4]School of Chemistry and Chemical Engineering, University of Southampton, Highfield Campus, Southampton, United Kingdom. [5]Institute for Life Sciences, University of Southampton, Highfield Campus, Southampton, United Kingdom. [6]Paul Langerhans Institute Dresden (PLID) of the Helmholtz Center Munich, University Hospital and Faculty of Medicine Carl Gustav Carus, Technical University Dresden, Dresden, Germany. [7]German Center for Diabetes Research (DZD), Neuherberg, Germany. [8]Max Planck Institute of Molecular Cell Biology and Genetics, Dresden, Germany. ***Corresponding author. Email: madhavi.krishnan@chem.ox.ac.uk**
†These authors contributed equally to this work.

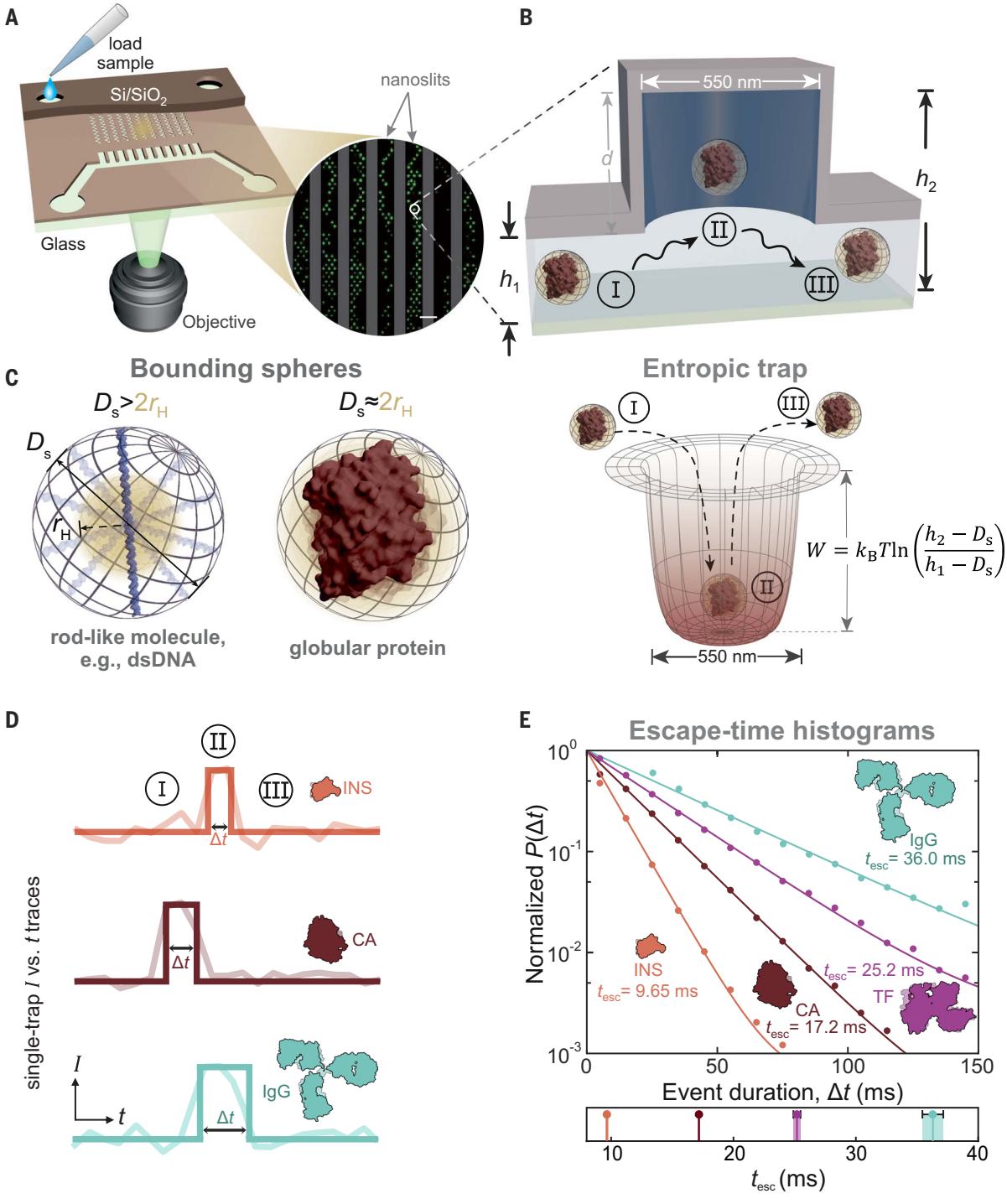

Fig. 1. Principle and overview of escape-time stereometry (ETs) in solution. (**A**) Schematic representation of a microfluidic chip carrying a series of fluid-filled parallel-plate nanoslits in which arrays of geometric indentations create local entropic traps for freely diffusing fluorescently labeled molecules in solution. A widefield fluorescence microscopy image presents the central quarter of a typical field of view, time-averaged over 1 s, displaying ~25 molecules diffusing in the trap landscape. Scale bar, 5 μm. (**B**) (Top) Schematic depictions of a globular protein molecule entering (state I), residing in (state II), and leaving (state III) a nanostructured indentation of diameter 550 nm, depth $d \approx 220$ to 290 nm, and height $h_2 = h_1 + d$ nm, located in a nanoslit of height $h_1 = 20$ to 70 nm. (Bottom) Corresponding entropic potential well of depth W in which molecules reside for an average time given approximately by $t_{esc} \propto r_H \exp(W/k_B T)$, where r_H is the hydrodynamic radius, k_B is the Boltzmann constant, and T is the absolute temperature. (**C**) Graphic representation of bounding spheres (gray) of diameter D_s, enclosing a rod-like dsDNA molecule (left) and a globular protein molecule (right). r_H (yellow sphere) can be considerably smaller than $D_s / 2$ for a nonspherical molecule, in contrast to a globular molecule. D_s and r_H values for a given species may be computed from a molecular structural model (as described in supplementary text S5.2). (**D**) Intensity versus time trace of each trap locus in the lattice permits identification of molecular residence or escape events of duration Δt. Representative events detected using a step-finding algorithm (dark lines) superimposed on raw traces. Three typical escape-time events for insulin (INS), carbonic anhydrase (CA), and immunoglobulin G (IgG), illustrating that Δt depends on the molecular weight of the species. (**E**) Probability density distributions $P(\Delta t)$ versus Δt for $N = 10^4$ to 10^6 recorded escape events fit to the form $P(\Delta t) \propto \exp(-\Delta t / t_{esc})$ to extract means t_{esc} values. For visual comparison across samples, the fitted t_{esc} values in each case are presented as vertical lines and symbols, with the measurement precision (given by the fit error) represented by a band on the reported mean value of thickness ± 1σ (bottom).

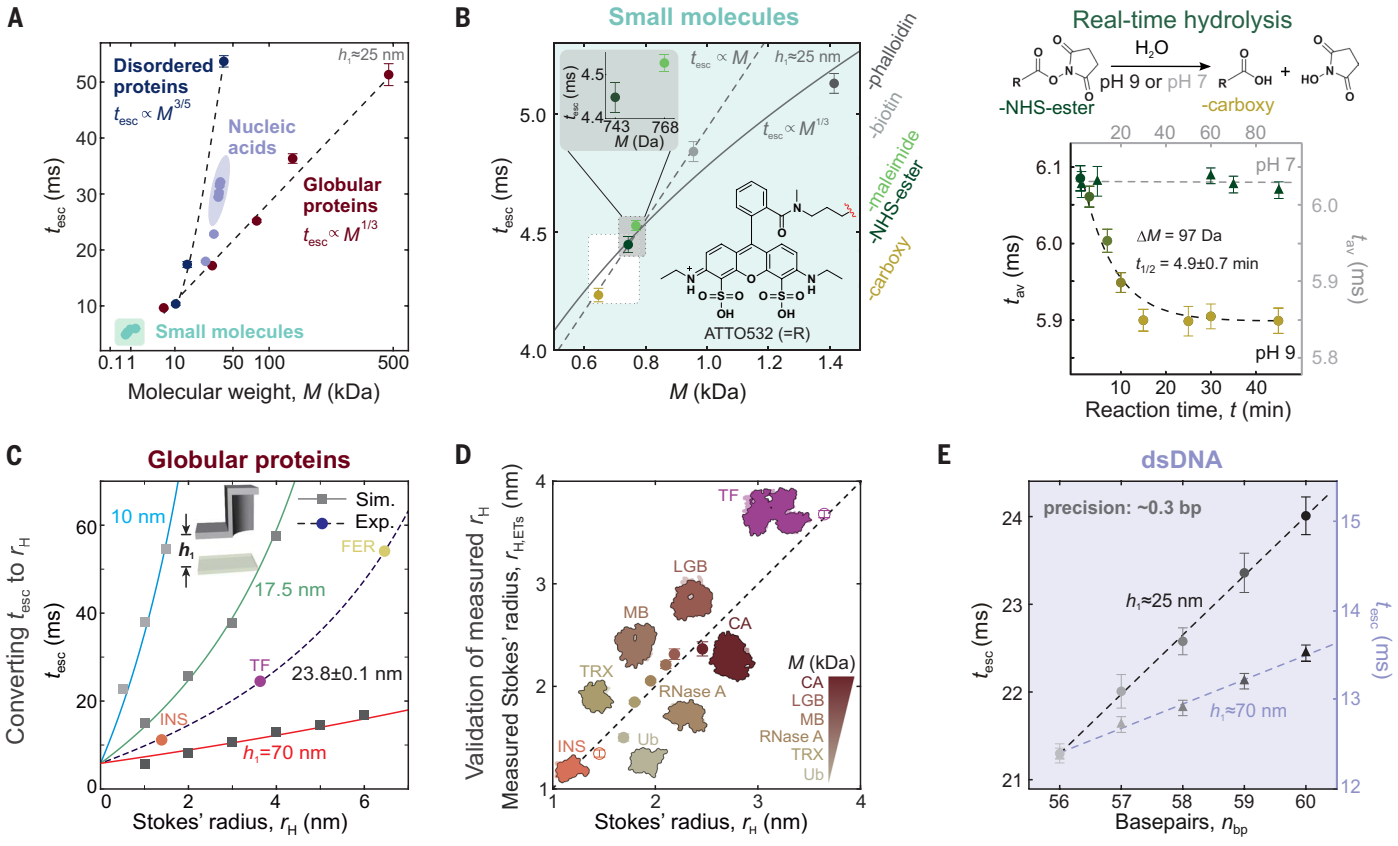

Fig. 2. Sensitivity of measured escape times to molecular weight. (**A**) Measurements of escape time t_{esc} versus molecular weight, M, presented on an abscissa scaled to the power of 1/3, and covering approximately three orders of magnitude, including small organic molecules (green symbols), globular proteins (brown symbols), disordered proteins (blue symbols), and dsDNA (purple symbols) in a device with $h_1 \approx 25$ nm. Globular proteins (insulin, carbonic anhydrase, transferrin, anti-insulin IgG, and apoferritin) and disordered proteins (*3*) (Starmaker-like, Stm-l; prothymosin α, ProTα; and a 13-mer proline-rich polypeptide sequence given in table S2) reveal good agreement with scaling behaviors $t_{esc} \propto M^{1/3}$ and $M^{3/5}$, respectively. (**B**) (Left) Plot of t_{esc} versus M for small fluorescent organic molecules represented by different chemical derivatives of the fluorophore ATTO532. The data display reasonable agreement with the $r_H \propto M^{1/3}$ expectation for small molecules (gray solid curve) (*66*). A linear trendline (dashed line) over a narrow range of M illustrates how ~0.5% measurement precision on t_{esc} implies the ability to detect differences of ~10 Da in the 1-kDa molecular weight regime. (Right) Real-time tracking of the hydrolysis of the NHS ester derivative into the carboxyl form entails a change in molecular weight of 97 Da. The 3% overall change in t_{av} over the course of the reaction is much larger than the measurement precision of ~0.5% in a 1-min-long measurement window permitting rate of hydrolysis to be measured at pH 9 (details in supplementary text S4.2). (**C**) Measured t_{esc} values may be converted to r_H and D_s values describing the molecular species using BD simulations (as described in supplementary text S5.1). Simulated values for spheres of radius r_H (square symbols) in a device with $d = 300$ nm illustrate the increasing nonlinearity of the measured response with decreasing h_1 and are well fit by the calibration function (Eq. 1) with $A \approx 0.3$ s/μm and $t_o = 5.83$ ms, which is used for all protein experiments (red, green, and blue curves). An example calibration measurement to determine the value of h_1 of the experimental device is performed using insulin (INS, orange), transferrin (TF, purple), and apoferritin (FER, yellow), whose Stokes' radii, r_H, are taken from molecular structures (as outlined in supplementary text S5.2). Measured t_{esc} data are fitted with the calibration function yielding $h_1 = 23.8 \pm 0.1$ nm, which agrees with the nominal design value of $h_1 \approx 25$ nm (dashed curve). (**D**) r_H values measured for a test set of proteins in the range $M = 10$ to 30 kDa compare well with theoretical expectations, as well as with measurements using fluorescence correlation spectroscopy (FCS) (fig. S10 and table S4). Filled symbols: Ub, ubiquitin; TRX, thioredoxin, RNase A, ribonuclease A, MB, myoglobin; LGB, β-lactoglobulin; CA, carbonic anhydrase; open symbols indicate INS and TF calibrator molecules. (**E**) Single–base pair differences in dsDNA in the range of 56 to 60 bp are clearly distinguishable, with the magnitude of measured differences increasing strongly with decreasing h_1.

statistically dominated measurement imprecision depends on N, the number of escape events observed, as $1/\sqrt{N}$. A large value of $N = 10^4$ to 10^5, achieved with highly parallel observation of the escape process at a molecular concentration of about 100 pM, implies ≤ 1% measurement imprecision on r_H, and is key to high-precision measurement (fig. S7 and supplementary text S1.1). We currently achieve quantitative detection of a labeled species down to ~10 fM in a 10-min continuous-flow measurement, with opportunity for improvement by at least a factor 100 through optimization of device design (fig. S5).

Measuring t_{esc} on a range of molecules spanning three orders in molecular weight, we noted the scaling $t_{esc} \propto r_H \propto M^{1/3}$ as expected for globular molecules, which implies that < 1% imprecision on t_{esc} translates to < 3% measurement imprecision in molecular weight (Fig. 2A). By contrast, for disordered proteins, e.g., prothymosin-α (ProTα) and Starmaker-like protein (Stm-l), we measure larger escape times that are in agreement with the scaling relationship $t_{esc} \propto r_H \propto M^{3/5}$ that is characteristic of unstructured polymers (Fig. 2A and fig. S9) (*25*–*27*).

Examining escape times for a range of small-molecule chemical derivatives of the fluorophore ATTO532 (molecular weight, $M \lesssim 1$ kDa), we note that ~0.5% measurement imprecision on the escape time, t_{esc}, implies the theoretical ability to detect differences of about a single carbon atom between molecular species, as shown in Fig. 2B (fig. S9). We demonstrate the ability to clearly distinguish a molecular weight difference of 25 Da between the *N*-hydroxysuccinimide (NHS) and maleimide derivatives of the fluorophore ATTO532 (figs. S1 and S9). The NHS ester of ATTO532 hydrolyzes in water to form carboxyl-ATTO532 and a leaving

NHS group, with the rate of hydrolysis strongly accelerated under alkaline conditions (*28*). Continuous-flow monitoring of the escape process for an aqueous solution of ATTO532-NHS (M = 743 Da; fig. S1) at pH 7 and pH 9 performed as a series of intermittent measurements of 30 s duration yielded average escape times t_{av} over all recorded escape events of duration Δt (Fig. 2B, right panel). A systematic overall reduction of 3% in t_{av} measured over the course of ~10 min implies a mass change of about 100 Da, commensurate with that of the NHS leaving group. The measured decay rate constant of 2.3×10^{-3} s^{-1} at pH 9 corresponds well to reported half-life values of ~5 min (supplementary text S4.2) (*28*). Real-time tracking of a change in molecular weight due to hydrolysis illustrates the power of both the speed and precision of the approach.

Nanoscale confinement offers nonlinear sensitivity of the readout to molecular size and shape

The measured t_{esc} values can be used to quantitatively infer molecular hydrodynamic radii, r_H, and bounding sphere diameters, D_s. To do so, we performed Brownian dynamics (BD) simulations of the escape process for spheres of radius r_H and bounding sphere diameter $D_s = 2r_H$ as described previously (supplementary text S5.1) (*29*). Simulated average escape times indeed display good agreement with the simple model outlined in the supplementary text (S3) and are captured by the following equation:

$$t_{esc} = Ar_H\left(h_2 - D_s\right) / \left(h_1 - D_s\right) + t_o \quad (1)$$

with the coefficient $A \approx 0.3$ s/μm accounting for the viscosity, device geometry, and various aspects of the imaging-based detection process, and an offset $t_o = 5.83$ ms $\approx t_{exp}$ (fig. S8). Thus, in a typical experiment, we first use globular proteins of known r_H to determine h_1 from fits of the data to Eq. 1; then we use this calibration function to convert the measured t_{esc} for a test molecular species to hydrodynamic radius r_H (fig. S10 and supplementary text S5.3). Inferred r_H values for a set of globular proteins measured in slits of calibrated height $h_1 = 23.8$ nm agree well with values computed on the basis of molecular structures, using the program HYDROPRO (*14*) (Fig. 2D, table S4, and supplementary text S5.2).

Equation 1 does indicate that, owing to rotational diffusion, molecules of nonspherical shape may exhibit a further enhancement of t_{esc} compared with their spherical counterparts of similar hydrodynamic radius. Because rotational times are generally much faster than translational diffusion, we may assume that a molecule that rotates isotropically while translating sweeps out a local volume defined by a sphere of minimum diameter $D_s > 2r_H$, as shown in Fig. 1C. Indeed, the method's high sensitivity to the molecular envelope is illustrated in our ability to clearly distinguish differences of 1 base pair (bp) (~3.4 Å) between rod-shaped double-stranded DNA (dsDNA) fragments in the size range $n_{bp} = 56$ to 60 bp (~20 nm in length) (Fig. 2E).

To test this ability further, we performed measurements on dsDNA and dsRNA of length $n_{bp} = 30$ to 60 bp, entailing lengths in the range 7 to 21 nm (supplementary text S5.4). Performing measurements of t_{esc} in slits of depth $h_1 \approx 25$ nm, we found a progressive nonlinear increase in t_{esc} with r_H values of the molecular species compared with the expectations for spheres of the same hydrodynamic radius r_H (fig. S11). Fitting the measured t_{esc} versus n_{bp} data using Eq. 1, assuming $D_s = bn_{bp}$, and using theoretical expressions for r_H for cylinders, we obtained a rise per base pair of $b \approx 3.2$ Å for the B-form double helix characteristic of dsDNA and $b \approx 2.3$ Å for the A-form double helix expected for dsRNA (Fig. 3A and fig. S11). These values are remarkably close to those inferred from high-resolution structural measurements and previous solution phase structural studies (3.32 ± 0.19 Å for B-DNA and 2.3 Å for A-DNA) (*18*, *30*).

Inferences on DNA-nanostructure size and shape

Because we expect ETs to offer strong and tunable shape-based discrimination of molecules that may be effectively identical in all other relevant respects (e.g., in hydrodynamic radius, mass, and charge), we studied DNA nanostructures that carry the same number of base pairs but differ in three-dimensional (3D) conformation (supplementary text S5.5) (*23*, *31*, *32*). We considered DNA nanostructures composed of 240 bases in states referred to as "bundle" and "square-tile" as previously described (*23*) (Fig. 3B), where $D_s \approx 20$ nm for the bundle provides an estimate of the size regime of the measurement. The "bundle" and "tile" are indistinguishable in diffusion coefficient measurements by fluorescence correlation spectroscopy (FCS) (table S5) (*23*). We performed t_{esc} measurements on both species in slits of height $h_1 \approx 100$, 70, and 40 nm (Fig. 3B). The relative insensitivity of t_{esc} to molecular conformation in the regime $h_1 \geq 70$ nm largely reflects a response expected based on pure diffusion alone. However, we observe systematically increasing t_{esc} values, with disparities between the two DNA nanostructures reaching a factor of 1.2 as h_1 decreases and approaches D_s. The measurement mode may thus be tuned to enhance the sensitivity of the escape-time readout to molecular 3D conformation, reflected in D_s, as suggested by Eq. 1.

According to Eq. 1, measurements performed with two different values of h_1 ought to support a readout of two properties of the molecule, namely r_H and D_s. We used t_{esc} measurements in slits of two different mean-calibrated height values of $h_1 = 41.4$ nm and 73.9 nm to infer these conformational parameters for the "bundle" and "tile" (fig. S12). Figure 3C provides a graphic representation of the procedure behind such an inference. A pair of independent measurements using sufficiently different h_1 values yields two curves on a plot of D_s versus r_H, whose point of intersection reflects the r_H and D_s values describing the molecular state. Comparing our inferences with values expected from molecular structural models obtained from coarse-grained molecular dynamics simulations using oxDNA and verified using SAXS (*32*, *33*) does reveal good mutual agreement (Fig. 3C, table; and fig. S12). For example, although the measured r_H values for the "tile" and "bundle" are rather similar, their D_s values are different and appear to be entirely responsible for the measured disparity between the two species.

Resolving mixtures of molecular conformational states by constructing single-molecule spectra

Escape-time data examined at ensemble level as shown in Figs. 1, 2, and 3 can reveal multiple escape timescales, depending on the sample (fig. S6 and supplementary text S2.2). A multitude of timescales generally contains important information on the sample, reflecting, e.g., heterogeneous states of multimerization or distinguishable 3D conformational states in monomeric molecules. Extracting these time components and their abundances in ensemble measurements can under certain conditions be subject to mathematical difficulties (*34*). Accessing information at the level of individual molecules not only avoids potential ambiguities of multiexponential fitting but can also furnish insight into the nature of the underlying states, e.g., whether they stem from individual molecules characterized by distinct 3D conformations that are stable over the observation window or rather from faster interconversion between different conformational states. Because we observe the hopping dynamics of every individual molecule in the microscope's field of view, we may indeed construct spectra of mean escape times reflecting single-molecule properties in a mixture of different molecular species or states as shown in Fig. 4. Performing measurements at low sample concentrations (~10 pM) permits facile recognition of trajectories arising from individual molecules whose average escape time now describes the conformational properties of individual molecular states (Fig. 4A, movie S2, and supplementary text S6.1).

We first validated the ability to identify, distinguish, and quantify stable single-molecule states by examining an equimolar mixture of 24-bp and 60-bp DNA: two geometrically highly well-defined and conformationally stable species (Fig. 4B, fig. S16, and supplementary text S6.2). We constructed single-molecule spectra by recording the average

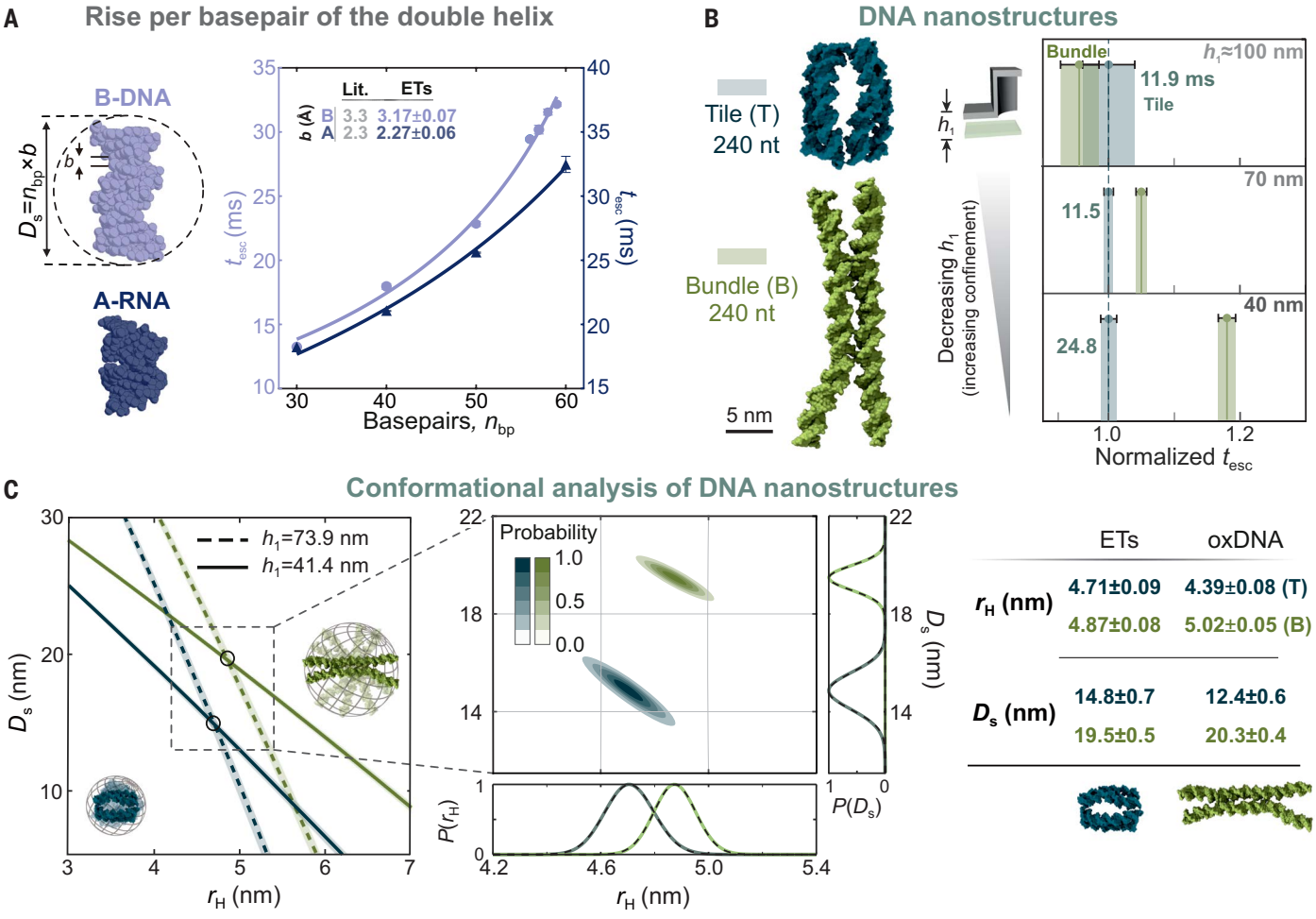

Fig. 3. Sensitivity of the escape-time readout to molecular shape (3D conformation). (**A**) Measurements of escape time t_{esc} versus number of base pairs, n_{bp}, for a series of dsDNA (B-form double helix) and dsRNA (A-form helix), fitted with Eq. 1 yielding $A = 0.35 \pm 0.01$ s/μm for RNA, 0.18 ± 0.01 s/μm for DNA, and rise per base-pair values, b, that are in good agreement with literature (Lit.) values from high-resolution structural methods (*30*). (**B**) DNA nanostructures composed of an identical number of nucleotides (nt) but in different 3D conformations of a "square tile" and "bundle" display increasingly separated measured t_{esc} values with decreasing slight height h_1. (**C**) Graphical representation of the solution of Eq. 1, using t_{esc} measurements for two different mean-calibrated values of h_1 (solid and dashed lines; see supplementary text S5.5 for details). Shaded bands around lines reflect the precision of the t_{esc} measurement. Region of intersection of the two uncertainty-broadened lines yields estimates of D_s and r_H for each nanostructure (left) and Gaussian probability density distributions of molecular physical properties $P(D_s, r_H)$, $P(r_H)$, and $P(D_s)$ (middle). Dashed superimposed curves demonstrate that the widths of the distributions reflect the statistical uncertainty on t_{esc} measurement and do not stem from detected conformational flexibility of the nanostructures. (Right) Table comparing ETs measurements with inferences from coarse-grained structures simulated using oxDNA (see supplementary text S5.5 for details).

escape time t_{av} for a number of single-molecule hopping trajectories, each consisting of N_{hop} escape events of varying duration Δt. Each t_{av} measurement in the resulting molecular escape spectrum thus represents an average value originating from a separate molecule. At present, we routinely record about $N_{hop} = 200$ to 300 hops from a molecule before either the label photobleaches or the molecule diffuses out of the field of view. Such a measurement implies a percentage measurement imprecision on t_{av} approaching $1/\sqrt{N_{hop}} \approx 5$ to 7% on a single molecule. This quantity also reflects the fractional standard deviation, σ/μ, of Gaussian distributed t_{av} values with mean μ, measured for a number of single molecules, N_{mol} (as shown in Fig. 4, B and D), and governs the ability of the method to resolve two closely separated molecular escape-time states (Fig. 4B and fig. S15). By contrast, the measurement imprecision on mean t_{av}, is approximated well by the SEM, $\sigma/\sqrt{N_{mol}}$, and can be minimized by measuring a large number of single-molecule trajectories (supplementary text S6.1). A wider field of view combined with a lower incident power density will support recording of longer single-molecule tracks ($N_{hop} > 10^3$), which could take the resolution σ to ~1 to 2% (*35*), simultaneously enhancing both molecular throughput (N_{mol}), which currently stands at a few hundred molecules, and measurement precision (Fig. 4D). Trajectory-based measurement of the mixture of dsDNA species indeed displayed two peaks in the molecular escape-time spectrum at mean molecular t_{av} values given by μ_1 and μ_2 of fractional abundances $m_1 \approx m_2 \approx 50\%$, that were in agreement with the corresponding values obtained from a biexponential fit of the same data in the ensemble approach (Fig. 4B, bottom row).

3D conformation of a riboswitch in aqueous solution

Like proteins, RNA can fold into well-defined 3D structures to carry out a wide range of cellular functions, but structure determination and prediction for RNA has lagged behind their protein counterparts (*36*). We used ETs to examine the solution phase 3D conformation of the SAM-IV riboswitch, whose structure has been recently solved by cryo–electron microscopy (cryo-EM) (figs. S13, S17, and S18, and supplementary text S5.6) (*37*).

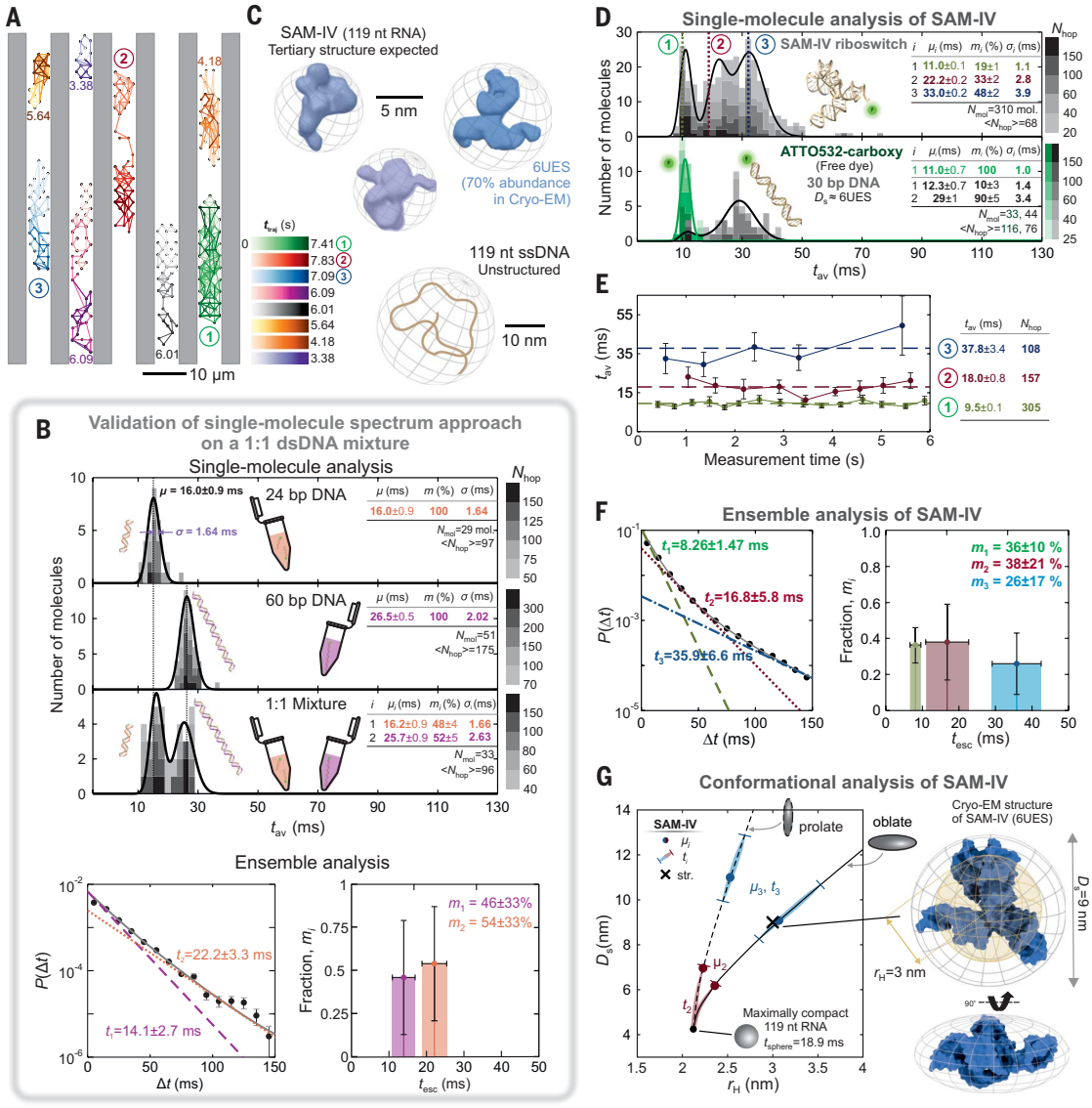

Fig. 4. Single-molecule spectra of SAM-IV riboswitch conformation and comparison with a structural model. (**A**) Schematic depiction of measured individual molecular trajectories of the SAM-IV riboswitch diffusing in a landscape of entropic traps in slits of height $h_1 \approx 20$ nm. The time evolution of each trajectory is indicated by the color intensity, which is scaled relative to the total trajectory duration t_{traj}, typically 2 to 10 s. Numerals 1, 2, and 3 denote example single-molecule trajectories of similar duration t_{traj}, ~7 s, but of rather different average escape times, t_{esc}, reflecting the three distinct states detected in the sample as shown in (D) and (E). (**B**) (Top) Validation of the single-molecule escape-time spectrum approach on a 1:1 mixture of 24-bp and 60-bp DNA. Each integer entry in the histogram corresponds to the average escape time, t_{av}, recorded for one molecular trajectory, with the gray level denoting the observed number of hops, N_{hop}. Pure 24-bp and 60-bp DNA samples show single peaks of average times, $\mu \approx 15$ and 26 ms, respectively, and the mixture displays two components of approximately equal fractional weight, m_i. Fits of the spectra are performed according to eq. S24 (black curve; see supplementary text S6.1 for detail). (Bottom) The same single-molecule trajectory data pooled and fit with a biexponential reveals two timescales and fractional weights that agree within error with the single-molecule trajectory analysis. Measurement precisions on the characteristic timescales are well estimated by the SEM and are captured by the fit errors on μ_i and t_i in the single-molecule and ensemble approaches, respectively. (**C**) Multiple possible 3D conformations reported for the SAM-IV riboswitch compared with a 119-nt unstructured ssDNA (fig. S13). (**D**) (Top) Single-molecule spectra of the SAM-IV riboswitch, accompanied by (bottom) superimposed spectra of ATTO532-carboxy dye and 30-bp DNA. Fitted timescales and component fractions μ_i and m_i in each case permit assignment of species and molecular states to the three inferred peaks in the ETs spectrum of SAM-IV. State 1 maps on to free dye, also present in other nucleic acid samples ($\mu_1 \approx 12$ ms). Two distinct conformations attributable to SAM-IV (states 2 and 3) are much more compact than the unstructured 119-nt ssDNA control (fig. S18), and display μ_i values similar to 30 bp DNA. (**E**) Recorded time traces of sequential escape events Δt, averaged over 16 consecutive escape events, for molecules 1, 2, and 3, display distinct and stable overall average values t_{av} over the >6-s measurement duration. (**F**) Ensemble measurements and corresponding multiexponential fit of $N = 4.4 \times 10^4$ escape events of SAM-IV reveal three timescales, t_i, and weight fractions that capture the timescales and molecular fractions detected in the single-molecule spectra. Comparing SEM values on the measured average t_i with those on the corresponding μ_i values in (D) illustrates how the measurement precisions delivered by the single-molecule trajectory approach outstrip the ensemble approach even though the trajectory approach relies on half the number of total recorded events ($N = 2.1 \times 10^4$). (**G**) Theoretical (D_s, r_H) plot for objects of fixed volume 40 nm^3—corresponding to an RNA molecule with $M = 38.51$ kDa characterizing SAM-IV—presents limiting cases for oblate (solid line) and prolate ellipsoids (dashed line), which intersect at a point given by the most compact, spherical state corresponding to an escape time $t_{sphere} = 18.9$ ms (see supplementary text S5.6 for details). Measured escape times and associated uncertainties shown in (D) and (F) imply (D_s, r_H) values as follows: Values from single-molecule measurement μ_3 (blue symbol) and the mean ensemble–fit timescale t_3 (blue shaded zone) indicate (D_s, r_H) coordinates describing a structure centered on either the oblate or prolate curves. Inferred coordinates for an oblate ellipsoid lie very close to the point characterizing the cryo-EM structure (PDB code: 6UES; black cross). Timescale μ_2 (red symbol) is consistent with a more compact state, on either the "oblate" or "prolate" curves, with red shaded regions corresponding to indications from ensemble-measurement value t_2.

Rather than a single timescale corresponding to the predominant cryo-EM structure (70% abundance, Fig. 4C), we found that both ensemble-averaged measurements and single-molecule spectra of the fluorescently labeled SAM-IV riboswitch revealed three distinct escape timescales (Fig. 4, D to F, and fig. S18). Examination of individual molecular trajectories revealed average molecular escape times falling into three distinct classes over the ~6-s measurement window, indicative of stable molecular conformations rather than rapid interconversion between states (Fig. 4, D to F, and fig. S17). To benchmark the observed timescales, we performed control measurements on free fluorescent dye, 30-bp dsDNA, and a 119-nucleotide (nt) single-stranded DNA (ssDNA), all of which entail little or no secondary structure (Fig. 4, C and D, lower panels; fig. S18; and supplementary text S6.3). The smallest timescale, $\mu_1 \approx t_1 = 10$ ms, in both the single-molecule spectrum and the ensemble measurements of SAM-IV sample, can be attributed to free fluorescent dye molecules in the mixture, which are generally difficult to remove entirely. However, we attribute the second and third measured timescales to two different conformational states, or similar groups of states, of the SAM-IV molecule—one compact and the other more extended. The larger of the molecular timescales, μ_3, is similar to the timescale measured for 30-bp dsDNA, whose value of $D_s \approx 9.6$ nm in fact closely resembles that of the reported structure (*37*) (Fig. 4D). The smaller of the two observed SAM-IV timescales, μ_2, in turn is indicative of a conformation of ~60% abundance, suggesting an overall more compact and globular state. All mean timescales at the ensemble-level and single-molecule level are in good mutual agreement; i.e., $t_i \approx \mu_i$ (Fig. 4G). Figure 4G displays a summary of the conformation analysis where the main conclusions are (i) that the measurements $t_3 \approx \mu_3$ (Fig. 4G, blue symbol and shaded zone) are consistent with that of an oblate ellipsoid characterized by D_s and r_H values that are very similar to those computed for the cryo-EM structure (Fig. 4G, black cross) and (ii) that the observation $t_2 \approx \mu_2$ indicates a conformation characterized by an ellipsoid of smaller D_s and r_H than the reported structure (red symbols and shaded region).

Upon addition of a high concentration of the SAM ligand, the escape-time spectra remained comparatively unchanged, indicating the absence of a conformational change in the riboswitch upon ligand binding (fig. S18). This observation is in line with cryo-EM data as well as with observations on other riboswitch aptamers, e.g., SAM-I and lysine riboswitches that do not change conformation upon ligand-binding (*38*, *39*).

Measuring binding affinities and rates of intermolecular association and dissociation

Nucleic acid interactions

We next explore the capability of our approach in making rapid, quantitative measurements of intermolecular interactions in mixtures, as reflected in measured dissociation constants, K_d, as well as of on- and off-rates of binding, k_{on} and k_{off} (Fig. 5 and supplementary text S7.2 and S7.3). DNA hybridization provides a simple, tuneable system where intermolecular binding affinities can be varied substantially using single–base pair increments between complementary stretches, supporting comparisons of measurements not only with independent experimental techniques but also with theoretical estimates. We validated the measurement approach with fluorescent molecular "bait" represented by short strands of ATTO532-labeled ssDNA ranging in length from 7 to 15 bases hybridizing to the corresponding complementary sequence at the 5′ end of an ~200-base-long "scaffold" of unlabeled ssDNA (Fig. 5, A and B). Mixtures of the labeled oligo at a concentration of 0.02 to 1 nM, and unlabeled DNA at various concentrations, are incubated to equilibrium, loaded into the trap landscape, and their escape times recorded over a period of 1 to 5 min. Histograms of event durations reveal two dominant timescales: a short $t_1 \approx 10$ ms corresponding to the free labeled oligo and a longer $t_2 \approx 30$ ms corresponding to the oligo bound to the 200-base ssDNA (Fig. 5A). The fractional abundances of the two species $m_{1,2}$ are determined with biexponential fits and plotted as a function of the concentration of the unlabeled binding partner to determine the K_d value of the interaction (Fig. 5B, upper panel; and supplementary text S7.1, S7.2, and S7.5).

We observed a systematic increase in binding affinity with increasing oligo length, reflected in progressively decreasing measured K_d values, in good agreement with previous reports (Fig. 5D and supplementary text S7.5) (*40*). Although samples are incubated over timescales ranging from several hours to several days to ensure that the binding reaction reaches equilibrium, the $t_{1,2}$ measurements corresponding to one point on a plot displayed in Fig. 5B take about 1 to 5 min over the range of concentrations of unlabeled binding partner that are probed (fig. S19 and supplementary text S7.3). Furthermore, the speed of the readout can be harnessed to perform real-time monitoring of the sample after either the mixing of the two unbound species, or alternatively, after the addition of an unlabeled "chaser" binding partner to the bound complex (Fig. 5C, lower panel; fig. S20; and supplementary text S7.3) (*41*). Measuring the fractional abundances as a function of time, similar to what is shown in Fig. 2B, permits the measurement of off-rates and corresponding on-rates for the same reaction. We find that these measured rates yield measures of $K_d = k_{off}/k_{on}$ that are consistent with the equilibration-based measurement approach as well as with theoretically expected values (*40*, *42*) (Fig. 5C and supplementary text S7.5).

DNA-protein and protein-protein interactions

We further examined DNA-protein binding affinity measurements performed with a singly labeled dsDNA molecule binding to unlabeled restriction enzymes (Fig. 6A, fig. S22, and supplementary text S7.6) (*43*). Here, we added the unlabeled binding partner—the restriction enzyme EcoRI—at various concentrations to a fixed concentration of 0.25 nM of fluorescently labeled 24-bp DNA containing the enzyme recognition site. In general, binding systems that produce large shifts in t_{esc} of a factor 2 to 5 upon binding yield $P(\Delta t)$ histograms that are amenable to multiexponential fitting and the extraction of fractional abundances of the underlying species (Fig. 5A). We determined the bound fraction of DNA from fitting two timescales to the t_{esc} data, as described in Fig. 5, and obtained a value of $K_d \approx 1.5$ nM, which is in excellent agreement with the reported value of $K_d \approx 1$ nM (*43*). However, many binding reactions are associated with small changes in size or conformation of the complex, which implies small changes in t_{esc}, sometimes as low as 10% or less. Here, the similarity of timescales corresponding to the two molecular states can render robust extraction of two exponential components and their individual fractions from the escape-time data untenable (*34*). Therefore, rather than fitting escape-time histograms, we track the quantity t_{av}, which represents a simple average over all escape events of duration, Δt, in the mixture of the two interacting species (supplementary text S7.1). We applied this procedure to examine a well-characterized antigen-antibody interaction between human leukocyte antigen (HLA) isoform A*03:01 (HLA A*03:01) and W6/32, a mouse-derived pan-HLA class 1–reactive monoclonal antibody (figs. S3 and S22, and supplementary text S7.7) (*44*). Anti-HLA antibodies are important as clinical biomarkers for evaluation and monitoring of allograft rejection risks in cell and organ transplantation (*45*). Binding of the labeled HLA antigen ($M \approx 49$ kDa) to its antibody ($M \approx 150$ kDa) results in a 40% increase in t_{av} relative to that of the free, labeled bait. Analyzing the t_{av} data to determine the bound fraction, we obtained $K_d \approx 0.4$ nM for this interaction, in excellent agreement with reported values of $K_d \approx 0.4$ nM and $K_d \approx 0.7$ nM (Fig. 6B and fig. S22) (*21*, *46*). Furthermore, our measurement displays sensitivity to the HLA antibody at concentrations as low as < 100 pM, providing a general approach to detecting antibodies in solution. The measurements also shows that t_{av} alone can serve as an excellent quantitative measure of the fraction of fluorescent bait in the bound state, and this approach is utilized again in investigations involving direct detection of free insulin in solution, described next (fig. S21).

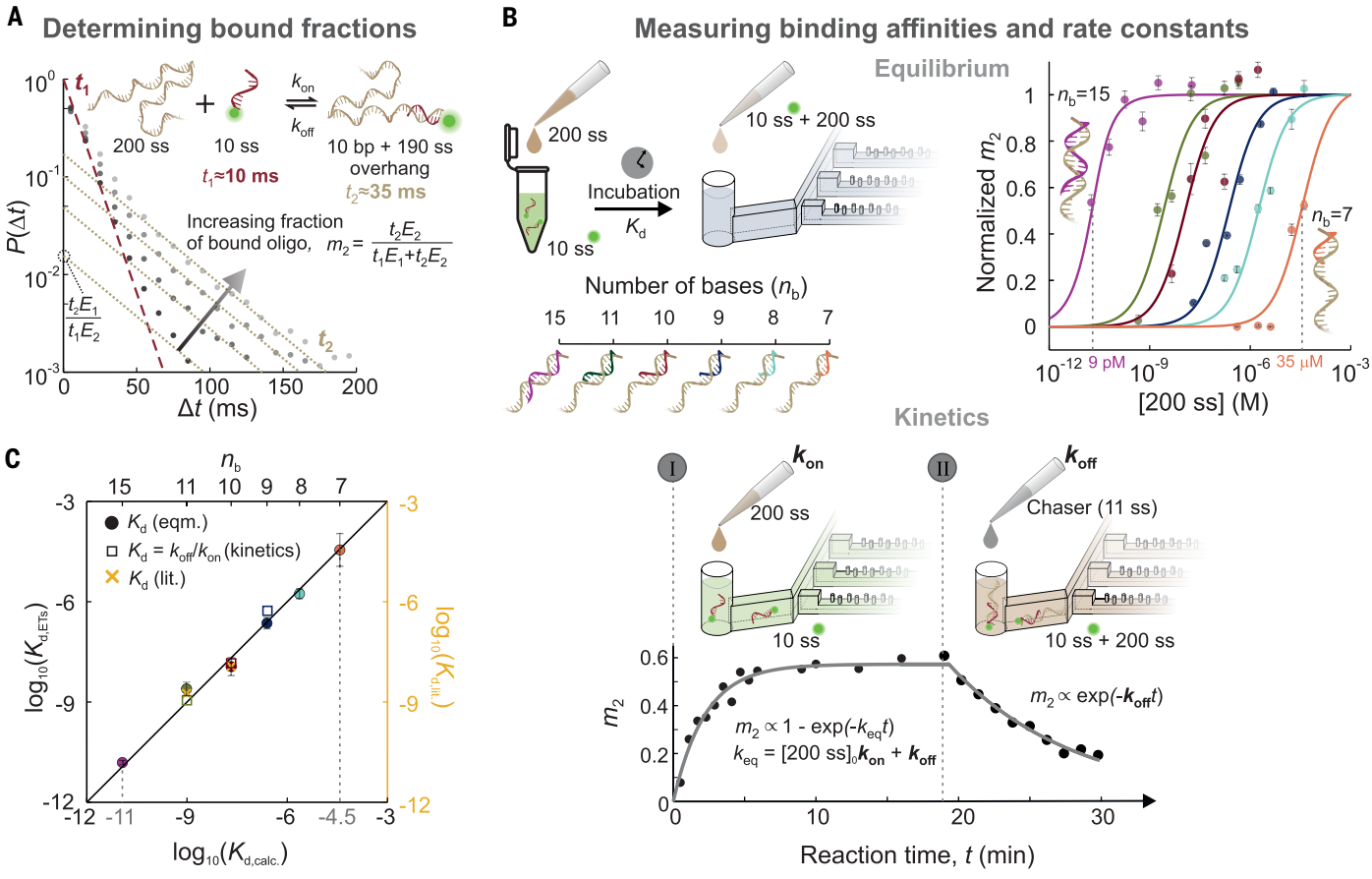

Fig. 5. Measuring association and dissociation rates and binding affinities in DNA hybridization. (**A**) Illustration of the experimental approach to determine the fractions of free and bound molecules in a bimolecular binding reaction. A labeled 10-nt ssDNA oligo binds to an unlabeled 200-nt ssDNA fragment. Incubation with a high concentration of 200-nt ssDNA shifts the free oligo timescale from $t_1 \approx 10$ ms to the fully-bound timescale $t_2 \approx 35$ ms. At intermediate concentrations, escape-time histograms obtained in 1-min-long measurements are fit with a biexponential holding t_1 and t_2 fixed to yield amplitudes of two exponentials reflecting the bound fractions m_1 and m_2. E_i denotes event fractions that are distinct from fractional species abundances, m_i (see supplementary text S7.1). (**B**) (Left) Measurements of m_2 after incubation of 0.02 to 1 nM of labeled oligo with 200-nt ssDNA of increasing concentration are fit with eq. S29 to obtain the affinity, K_d, of the interaction. (Right) Measurements for a range of oligos of length $n_b = 7$ to 15 bases demonstrate K_d measurements in the range 10^{-11} M to 10^{-4} M. (Bottom) Constructing $P(\Delta t)$ histograms of the reaction mixture in real time after mixing provides a measure of m_2 versus reaction time, t, which is fit with eq. S30 to obtain the effective on-rate constant k_{eq}. Equilibrated, fully bound mixtures of labeled oligo and 200-nt ssDNA are mixed with an excess of unlabeled oligo and the decaying bound fraction, m_2, measured as a function of time to yield the dissociation rate constant k_{off} using eq. S32. k_{eq} and k_{off} together determine the association rate constant, k_{on}, using eq. S31, from which K_d can be determined independently using eq. S33. (**C**) Measurements of K_d from both equilibrium (circles) and kinetic (squares) approaches compare well with theoretically estimated and literature values (crosses) over a range of nearly seven orders of magnitude (see supplementary text S7.5 for further discussion).

To explore the possibility of detecting a small, medically relevant protein analyte such as free insulin in a complex sample, we first examined the use of a fluorescently labeled 31-base insulin-binding aptamer (IGA3) that is expected to bind insulin in the folded G-quadruplex–containing state (*47*) (Fig. 6C). Upon formation of the structured state, ETs directly detects a 10% reduction in t_{av} for the aptamer (Fig. 6D and fig. S23). We incubated 5 nM of singly labeled, folded aptamer with 100 µM unlabeled insulin, which is well above the reported K_d of the interaction (*48*, *49*). We noted a 15% increase in t_{av} for the folded aptamer, which may be expected on the basis of the increase in mass of the complex alone. Notably, we measured no change in t_{av} for the unfolded aptamer in the presence of insulin, pointing to the apparent requirement of secondary structure in the aptamer for insulin binding (*47*). Measuring t_{av} for mixtures containing variable concentrations of free, unlabeled insulin and a fixed low concentration of labeled aptamer bait of 1 nM, we obtained a $K_d \approx 90$ nM, which is in broad agreement with literature values (supplementary text S7.8) (*48*, *49*). This measurement demonstrates a straightforward, rapid and general approach to detecting the presence of a small, medically important analyte in solution. However, the relatively modest affinity of the aptamer for insulin is a major limitation for direct insulin sensing at physiologically and biochemically relevant concentrations.

We therefore set out to characterize a higher affinity interaction for insulin by using a biologically relevant binding partner that is tuned to respond to low-nM physiological concentrations of insulin. The insulin receptor (IR) is a transmembrane receptor tyrosine kinase that is activated by insulin binding to its extracellular ectodomain (ECD) (*50*). We measured the binding affinity between a singly labeled insulin molecule ($M \approx 6$ kDa; fig. S2) and the soluble IR-ECD ($M \approx 280$ kDa) by ETs (supplementary text S7.9). The large disparity in timescales between free and bound insulin facilitates a direct measurement of bound fractions, using two fixed timescales in the ensemble fit (Fig. 6C and fig. S22). The highest affinity we measured for the interaction was $K_d \approx 7$ nM, which is smaller than the previously reported $K_d \approx 30$ nM value measured for the same IR-ECD by nano-differential scanning fluorimetry (*50*, *51*) and closer to the sub-nM high-affinity binding of the first ligand binding site of the full-length IR (*52*–*54*).

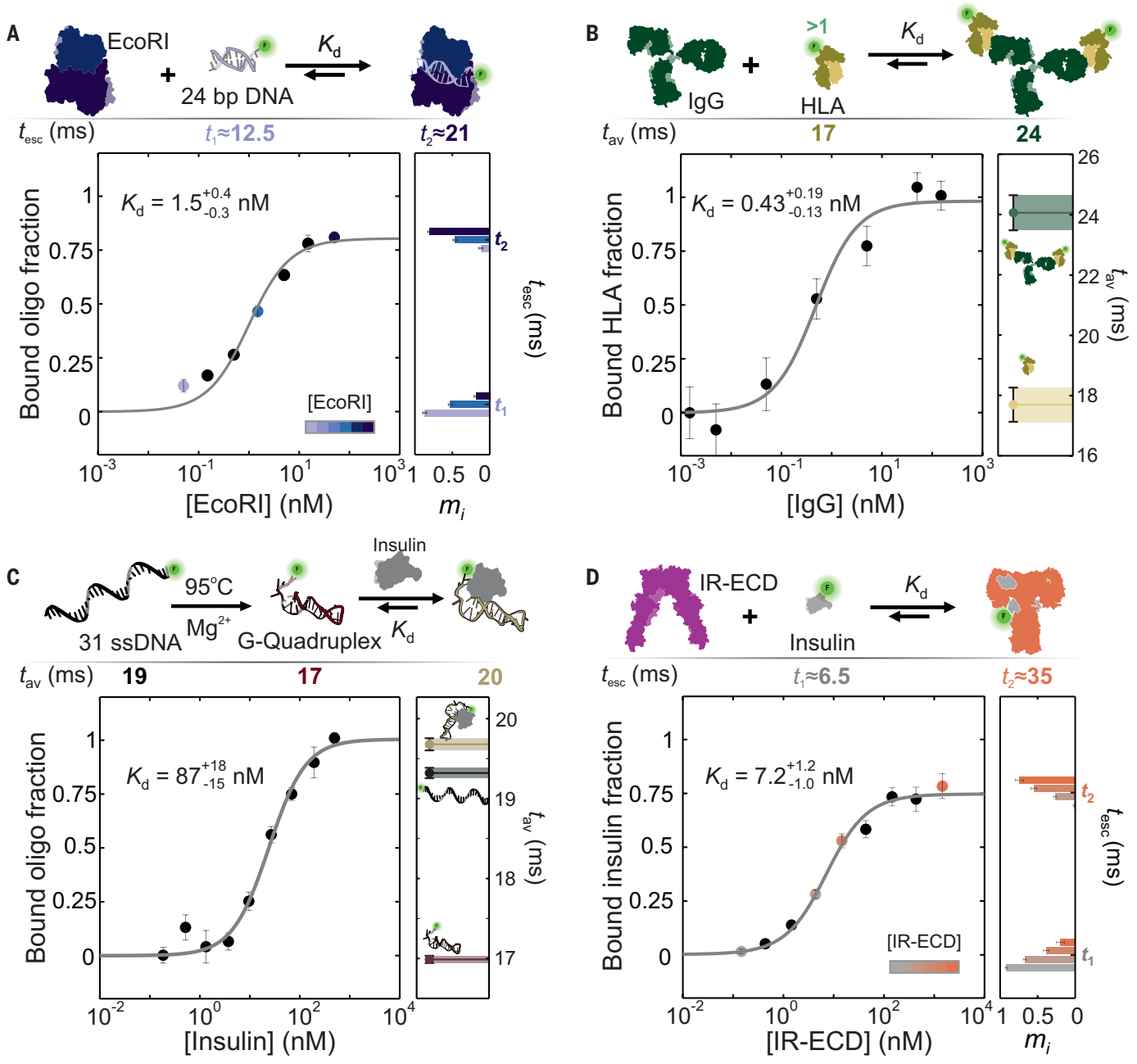

Fig. 6. Measuring binding affinities in DNA-protein and protein-protein interactions. When disparities in escape times characterizing the bound and free states, t_1 and t_2, are larger than a factor of two, the method shown in Fig. 5A can be used to determine m_2 and therefore K_d values for the interaction of (**A**) the restriction enzyme EcoRI (molecular weight ~28.5 kDa) with 250 pM of a labeled 24-bp DNA oligo (~15 kDa) carrying the restriction sequence, (**D**) the insulin receptor ectodomain (IR-ECD, 280 kDa) with 2 nM of fluorescently labeled insulin (~6 kDa). When the shift in timescale upon binding is much smaller (~5 to 10%), we use the average escape time, t_{av} as an indicator of m_2 (see fig. S21 and supplementary text S7 for more details). Using this method, we determine interaction affinities of (**B**) 100 pM of the fluorescently labeled HLA antigen (~48 kDa) with the corresponding immunoglobulin G (IgG, ~150 kDa). (**C**) Folding of the insulin-binding 31-base IGA3 aptamer results in a 10% reduction of t_{av} that subsequently systematically increases upon binding of increasing concentrations of insulin added to 5 nM of the aptamer. In all cases, the measured K_d values are in good agreement with the literature.

Structural inferences on the "apo" and "liganded" states of the IR-ECD

We then explored the general potential our platform for membrane protein receptor-based immunoanalysis and diagnostic applications. We used fluorescently labeled IR-ECD as bait to detect the much smaller, unlabeled insulin molecule in solution. IR-ECD is expected to bind up to four insulin molecules, entailing an increase in molecular weight of ~9% ($\Delta M \approx 25$ kDa) and a modest concomitant increase of ca. 3% in t_{esc} (or r_H) (*51*).

To examine the conformational properties of the apo- and liganded IR-ECD, we first carried out a structure and conformation analysis of IR-ECD in the insulin-free and bound states by using ETs (as described in Figs. 3 and 4). On the basis of structural data from cryo-EM, the soluble ECD of the IR is expected to have an approximate spatial extent

of 17 nm, a hydrodynamic radius of r_H = 6 nm, and can bind up to four insulin molecules. Molecular structures obtained with x-ray crystallography and cryo-EM indicate that upon insulin binding, the IR-ECD undergoes a substantial conformational change from an "inverted-V" apo-state to a fully liganded "T-state" including intermediate states with a lower number of bound insulin molecules (*51*, *55*), as also reported for snail venom insulin–human IR-ECD interactions (*56*) (Fig. 7A). However, the generation of crystal structures of IR-ECD in the apo state has relied on internal conformational stabilization. Indeed, the high degree of conformational flexibility of the apo state compared to its liganded counterpart has hindered identification of a representative 3D structure for the ligand-free state using cryo-EM (*51*).

We performed t_{av} measurements on 1 nM labeled IR-ECD, both in the absence and presence of insulin at a concentration of 100 nM, well above the expected K_d of the interaction (supplementary text S5.7). In contrast to the molecular binding measurements discussed in the previous section, all of which entailed an increase in size of the complex and therefore of t_{av} upon binding of the small, labeled ligand, here we found that t_{av} values of the fluorescent complex decreased by about 7% to 21 ± 0.1 ms compared to 22.5 ± 0.3 ms for the ligand-free species (Fig. 7A). Within our view of the underlying measurement principle, a decrease in t_{av} that occurs despite an increase in mass upon binding indicates a reduction in the overall spatial extent of the complex in the bound state. This strongly suggests that the readout is in fact dominated by conformational compaction of IR-ECD upon insulin binding. However, the x-ray structure of the conformationally stabilized apo state and the cryo-EM structure of the liganded state suggest very similar r_H and D_s values, which would entail negligible differences in t_{av} in our experiment, contrary to the experimental observations (Fig. 7A, top panel, and fig. S14).

To quantitatively explore the implied conformational difference between the two states of the receptor in solution, we repeated t_{av} measurements in slits of systematically smaller height in the range $h_1 \approx 30$ to 60 nm (Fig. 7A, lower panel, and fig. S14). Similarly to what we observed on the DNA nanostructures, we noted progressively larger disparities in t_{av} between the "apo" and liganded states, increasing from ~5% in the deepest slits to > 20% in the shallowest (Fig. 7A). The plots in Fig. 7B graphically represent permissible values r_H and D_s for the two molecular states, inferred from measurements at four different slit heights (fig. S14). The r_H and D_s values inferred from the intersection of lines representing a pair of measurements corresponding to mean values of h_1 = 38.7 nm and 62.6 nm show that the two states are well resolved, highlighting systematic differences $\Delta D_s = D_{s,lig.} - D_{s,apo} \approx 1.5$ nm and $\Delta r_H \lesssim 0.25$ nm. The uncertainty in determining the calibrated height h_1, which can be as high as ~3 to 4 nm in some cases, limits the level of accuracy on absolute values of some of our present readouts of r_H and D_s, but this can be improved upon in the future (Fig. 7C). Notwithstanding the current uncertainties in determining absolute values of r_H and D_s, we note systematic measured differences between the apo and liganded states that are relatively robust to uncertainties in h_1 (Fig. 7D). Furthermore, the analysis readily admits solutions for r_H and D_s that agree reasonably with the corresponding values characterizing the cryo-EM structure of the ligand saturated state [Protein Data Bank (PDB) code: 6SOF] for values of h_1 within the calibration error (Fig. 7, C and D, black symbol).

Taken together, our results indicate that the liganded state may indeed be more compact than the ligand-free "apo" state. Although the absence of a 3D structure of the apo state in solution precludes a quantitative assessment of our molecular property readouts against an independent structural model, our measurements do point to an apo state characterized by greater flexibility than the liganded state (Fig. 7C, right panels). Thus, in contrast to the binding of the aptamer bait to insulin, the smaller t_{av} value of the IR-ECD bait in the presence of insulin appears to be a direct consequence of conformational compaction as the IR-ECD transitions from the insulin-free apo state to the insulin-bound liganded state. This conformational compaction is large enough to offset the effect of a modest increase in mass (up to ~25 kDa) that occurs upon binding of up to four insulin molecules. The relative insensitivity of the hydrodynamic radius r_H of IR-ECD to the presence or absence of insulin is in broad agreement with diffusion measurements on the same samples using FCS, as well as with computational estimates based on the molecular 3D structures of the stabilized apo and liganded states (Fig. 7C, fig. S14, and table S4). Thus, the overall measured response is dominated by the conformational change in the receptor induced by ligand binding, as reflected in the reduced diameter of the molecular bounding sphere, D_s (Fig. 7, C and D).

Affinity-based detection of free insulin in serum

Lastly, Fig. 7E demonstrates a route to exploiting conformation changes in a receptor protein to detect analytes near physiologically relevant concentrations in complex samples. We first incubated 80 pM labeled IR-ECD with a range of insulin concentrations in PBS buffer for 1 hour at room temperature. Imaging the chip for about 5 min per incubated sample, we noted a gradual reduction in t_{av} with increasing insulin concentration, with the maximum and minimum timescales corresponding to those expected for the apo (22.5 ms) and liganded states (21 ms) in a slit of $h_1 \approx 40$ nm. Assuming that t_{av} is proportional to the amount of IR-ECD in the liganded state, we obtain $K_d \approx 2$ to 12 nM, which is in good agreement with the literature (*50*–*54*).

We then titrated insulin into simulated serum containing ~100 pM of labeled IR-ECD, incubated the samples for 30 min at room temperature, and assessed the binding, as indicated by t_{av} (fig. S24 and supplementary text S7.10). We found K_d values around 2 to 4 nM, supporting detection of free insulin at ≥1 nM in serum, which lies at the higher end of the typical physiological range (<1 nM). Similar measurements in a sample of true human serum, however, revealed a substantial conformation change with small amounts of added insulin, indicating an estimated $K_d \approx 100$ pM and demonstrating that the readout principle is not affected by the complex background of human serum (fig. S24 and supplementary text S7.10). Genetically modified and conformationally stabilized variants of IR-ECD are known to offer much higher affinities of $K_d \approx 80$ pM, comparable with the full-length IR (*57*, *58*). Given an affinity reagent with $K_d \leq 100$ pM, our ability to quantitatively measure t_{av} at femtomolar concentrations offers the subpicomolar detection sensitivity required for highly quantitative, rapid, and sensitive detection of analytes in ultrasmall volumes of serum or plasma in the picomolar regime (Figs. 5B, 6B, and fig. S5). The same detection principle may be applied to a host of diagnostic biomarkers, including small-molecule hormones and metabolites, and such detection assays may be run in a highly parallel spectrally multiplexed fashion.

Rather often, e.g., when metal ions or small molecules bind to proteins, molecular weight shifts can be miniscule compared with changes in shape and conformational properties (*59*). Posttranslational modifications such as phosphorylation, glycosylations, or DNA methylation may also be detected on the basis of changes in mass and/or conformation. ETs presents a versatile chip-based measurement platform that meets a variety of molecular analytical goals through highly conformation-sensitive detection under native conditions in solution. The same platform operated in "charge mode" enables state, structure, and chemical discrimination based on molecular effective charge as previously described (*3*, *18*, *19*, *23*). Although the spectral and photophysical properties of labels may be further leveraged to foster optical multidimensionality in the measurement (*60*–*62*), detection based on scattered light will support label-free measurements, potentially enabling simultaneous molecular weight inferences (*7*).

In fluorescence detection, the labeled species present at trace concentrations can act as a reporter of molecular or complex state in the presence of high background concentrations (mM) of unlabeled, interacting matter of any mass, identity, and compositional complexity. Thus, ETs may be well suited to the detection of multisubunit fragile macromolecular assemblies that form on account of weak interactions and

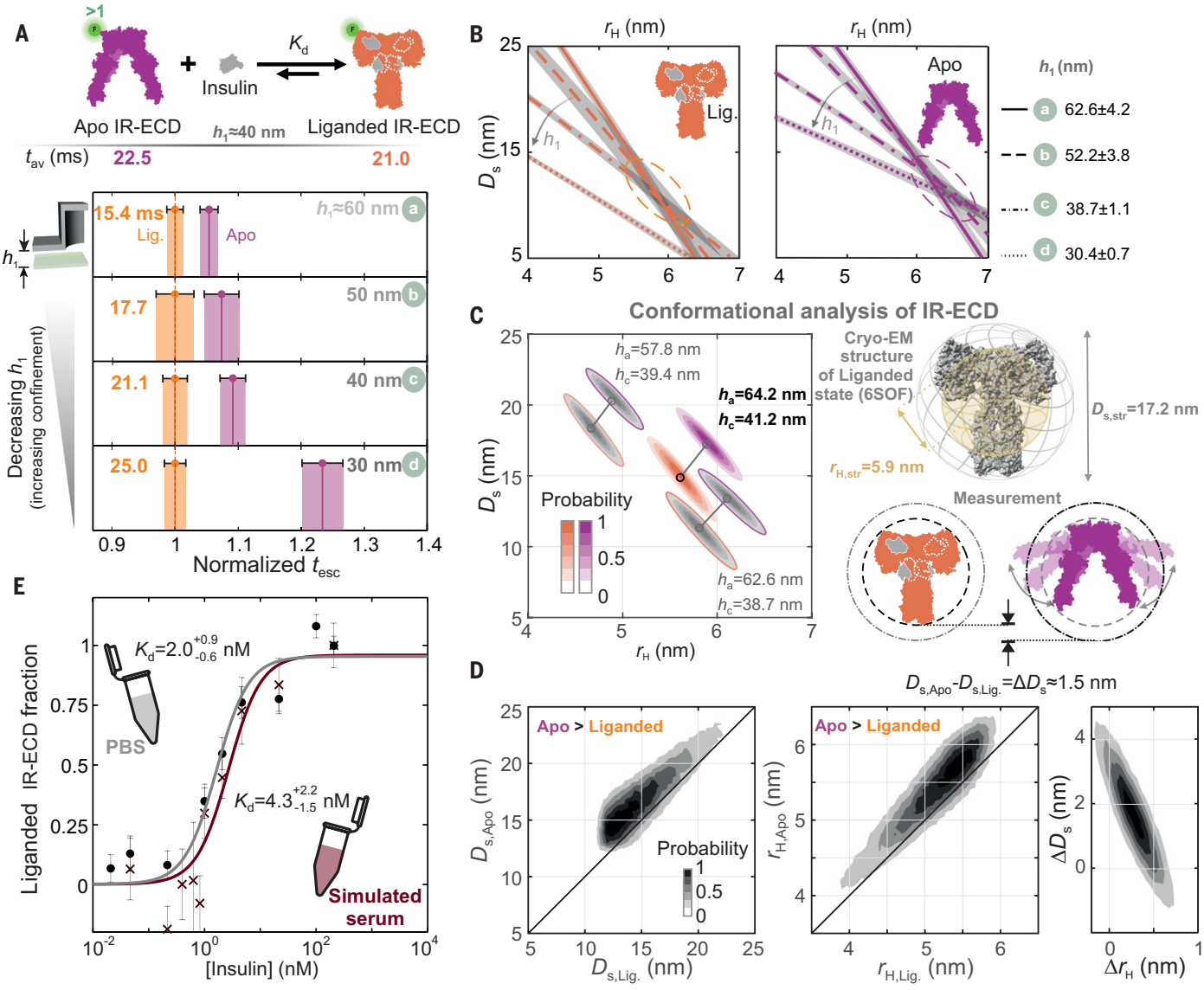

Fig. 7. Detection and structural modeling of conformational changes of the insulin receptor ectodomain (IR-ECD) upon insulin binding. (**A**) Upon incubation with 100 nM insulin, well above the expected K_d of the interaction reported in Fig. 6B, the fluorescently labeled IR-ECD displays a reduction in average escape time t_{av} from 22.5 ± 0.3 ms to 21 ± 0.1 ms in a device where $h_1 \approx 40$ nm, used for K_d measurements in (**E**). Examining the ligand-free "apo" and the liganded states of the IR-ECD in slits of height ranging from $h_1 \approx 60$ to 30 nm reveals progressively increasing fitted t_{esc} values for both states, as well as a systematically increasing ratio of the two timescales, clearly indicating differences in 3D conformation between the two states (plots a to d). (**B**) Graphical presentation of Eq. 1 for the liganded state (left) and "apo" state (right), using fitted t_{esc} values in slits with quoted h_1 values determined by calibration (fig. S14). Lines represent (D_s, r_H) solutions expected for h_1 corresponding to the mean value obtained from device calibration (see fig. S14). Shaded grey bands denote uncertainties given by the precision of the t_{esc} measurement. Similar to what is shown in Fig. 3, the intersection of any two bands gives the range of allowed values of (D_s, r_H), characterizing the molecular state. (**C**) (Left) Three possible sets of solutions describing the "apo" and liganded states obtained by assuming h_1 values that vary within 1 SD of the mean values measured for devices represented in (A), plots a and c. The true uncertainty in slit height (<~1 nm) is expected to be much smaller than that obtained by the calibration procedure (*3*). Although absolute values for D_s and r_H are not determined with high accuracy at present, the difference between the two states is systematic and points to an increase of $\Delta D_s \approx 1.5$ nm and $\Delta r_H \approx 0.25$ nm for the "apo" state compared with the liganded case. (Right) Conceptual view of the inferred conformational difference between the "apo" state (PDB code: 4ZXB) and the cryo-EM ligand saturated state (PDB code: 6SOF) as inferred from ETs measurements. (**D**) Plots of $D_{s,Apo}$ versus $D_{s,Lig.}$ and of $r_{H,Apo}$ versus $r_{H,Lig.}$ for several different pairs of h_1 values lying within the range inferred from calibration for the (a, c) device geometry pair represented in (A) and (B). The plots confirm a systematic compaction in overall extent of the liganded state compared with the ligand-free "apo" state (fig. S14). (**E**) Affinity measurement for the binding of the IR-ECD to insulin. The bound fraction is inferred from the reduction in average timescale t_{av} of labeled IR-ECD due to the conformational change upon insulin binding, as shown in (A) (see Fig. 6, fig. S24, and supplementary text S7.10 for details). Measurements in both PBS (black circles) and in simulated human serum (brown crosses) give similar K_d values that are consistent with the literature.

are challenging to detect with other methods (*63*). Rapid solution-phase direct sensing of complex formation may also benefit investigations of long-standing problems, such as pathological protein aggregation (*64*).

Lastly, the ability to map measurements of conformation onto molecular 3D structure-based computed quantities suggests that the ETs readout could aid machine learning approaches to molecular structural modeling, validation, and inference, contributing to tackling frontier problems in structural studies, e.g., the conformation of disordered proteins and RNA, including the ability to characterize rare states.

Materials and methods

Commercially obtained samples

Recombinant human insulin (INS, 91077C) was obtained from SAFC Biosciences, Andover, UK. Ubiquitin from bovine erythrocytes (Ub, U6253), Thioredoxin from *Escherichia coli* (TRX, T0910), Ribonuclease A from bovine pancreas (RNase A, R6513), Myoglobin from equine heart (MB, M1882), β-Lactoglobulin A from bovine milk (LGB, L7880), Carbonic anhydrase (CA, C7025), human apo-Transferrin (TF, T2036) and Apoferritin (FER, A3660) were all from Sigma-Aldrich, Gillingham, UK. Human insulin detector antibody (IgG, ab253508) was purchased from Abcam, Cambridge, UK. HLA-ABC monoclonal antibody W6/32 (IgG, 16-9983-85) and Human EGF Recombinant Protein (PHG0314) were from Thermo Fisher Scientific. HLA-A*03:01 RLRAEAQVK was provided by the NIH Tetramer Core Facility at Emory University, Georgia, USA. EcoRI (R0101M) was obtained from New England Biolabs. Nucleic Acid samples were mostly obtained from Integrated DNA Technologies Inc., Coralville, IA, with sequences shown in table S1. With the exception of the SAM-IV riboswitch sample, and reference DNA sample – synthesis of these is outlined in the following sections. All fluorescent dyes were obtained as lyophilized powder from ATTO-TEC GmbH, Siegen, Germany. The disordered proteins Starmaker-like (Stm-l), prothymosin α (ProTα), were obtained as described in (*3*). A 13-mer proline-rich polypeptide was obtained by custom synthesis from Bio-Synthesis Inc., respectively. Details of the sequences of these proteins can be found in table S2. Samples were generally prepared using UltraPure DI water (Invitrogen) and PBS (pH 7.4, Gibco). Samples, except for antibodies were aliquoted, flash-frozen and stored at either −20 or −80°C as per manufacturer's instructions.

Protein-labeling procedure

To protein stock solutions in DI water or PBS (pH 7.4), 1 M $NaHCO_3$ (Sigma-Aldrich) was added to a final concentration of 0.1 M in order to adjust the pH to 7.5 to 8.3. After addition of a molar excess of ATTO532 NHS-ester in DMSO or DI water, the reaction was incubated for 1 hour at room temperature, protected from light. Unreacted dye was removed by buffer exchanging twice into PBS (pH 7.4) using Zeba micro spin desalting columns with 7 K or 40 K MWCO (Thermo Fisher Scientific) following the manufacturer's instructions. Labeled insulin and dye were separated into PBS using size exclusion chromatography on a Superdex 75 10/300 GL column (Cytiva) on an AKTA pure protein purification system (Cytiva). Post-labeling concentrations and degree-of-labeling (DOL) were calculated from absorbance measurements at 280 and 532 nm on a Nanodrop spectrophotometer (Thermo Fisher Scientific), and are presented in table S3.

Electrospray mass spectrometry (ESI-TOF)

Reverse-phase chromatography on an Agilent 1100 HPLC system (Agilent Technologies, Palo Alto, CA, USA) was coupled in-line to a 1969 MSD-ToF electrospray ionization orthogonal time-of-flight mass spectrometer (Agilent Technologies Inc, Palo Alto, CA, USA). Samples were diluted to a concentration of 0.02 mg/ml (for insulin) or 10 μM (for ATTO532 dyes) in 0.1% formic acid. 50 μl were injected on to a 2.1 mm by 12.5 mm ZORBAX 5-μm 300SB-C3 guard column. The column oven was maintained at 40°C. Ultra-high purity water (Optima, LC-MS grade, Fisher Chemical) with 0.1% formic acid (Optima, LC/MS grade, Fisher Chemical) (solvent A) and methanol (Optima, LC/MS grade, Fisher Chemical) with 0.1% formic acid (solvent B) were used as mobile phases. Chromatography was started at 90% A and 10% B for 15 s, followed by a two-stage linear gradient from 10% B to 80% B over 45 s and from 80% B to 95% B over 3 s. Elution was performed isocratically at 95% B for 1 min 12 s followed by equilibration at 90% A and 10% B over 45 s. The flow rate was set to 1.0 ml/min. For mass spectrometry the instrument was configured with the standard ESI source and operated in positive ion mode. The capillary voltage was set to 4000 V and the nebulizer pressure to 60 psi. The source temperature was kept at 350°C with a drying gas flow rate of 12 liters/min. The ion optic voltages were: fragmentor 250 V, skimmer 60 V and octopole RF 250 V. Data analysis was performed using Agilent MassHunter Qualitative Analysis B.07.00 software (Agilent Technologies, Palo Alto, CA, USA), see figs. S1 and S2.

Native mass spectrometry method

HLA was desalted and buffer exchanged twice into 250 mM ammonium acetate using Zeba micro spin desalting columns with 7 K MWCO following the manufacturer's instructions and diluted to 10 μM. Spectra were acquired on a Q Exactive UHMR Orbitrap mass spectrometer (Thermo Fisher Scientific) with in-house prepared gold-plated capillaries using the following parameters: capillary voltage of 1.3 kV, capillary temperature of 100°C, in-source trapping of −10 V and HCD energy 1. Spectra were averaged and deconvolved using UniDec software (*65*), see fig. S3.

DNA nanostructure synthesis

Two DNA nanostructures were synthesized as described in (*23*). The "square tile" consists of four terminally tethered 30-bp dsDNA helices, and the "bundle" consists of two 60 dsDNA helices tethered at two points along the length of the helix. Both structures consist of 240 nt, and are labeled with a single ATTO532 dye.

SAM-IV riboswitch and reference DNA synthesis

ssRNA and DNA sequences, both 119 nt in length, were synthesized (sequence information in table S1) on an Applied Biosystems 394 automated DNA/RNA synthesizer using a standard phosphoramidite cycle of detritylation, coupling, capping, and oxidation on a 0.2 μmol scale. For DNA, TCA (3% in dichloromethane), 1*H*-tetrazole (0.45 M in acetonitrile), Cap A (10% acetic anhydride, 10% lutidine and 80% tetrahydrofuran) / Cap B (16% N-methylimidazole in tetrahydrofuran) and iodine (0.02 M in tetrahydrofuran, pyridine and water) were used. Pre-packed nucleoside SynBaseTM CPG 3000/110 (Link Technologies) resins were used and β-cyanoethyl protected phosphoramidites (dA-bz, dG-ib, dC-bz and dT where bz = benzoyl and ib = *iso*-butyryl, Sigma-Aldrich) were dissolved in anhydrous acetonitrile (0.1 M) immediately prior to use. The coupling time for dA, dC, dG and dT monomers was 45 s, and 600 s for the 5′-amino modifier phosphoramidite monomer. Stepwise coupling efficiencies were determined by automated trityl cation conductivity monitoring and were >98% in all cases.

For RNA, 2′-O-TC protected RNA phosphoramidites (A-bz, C-ac, G-ib, U, Sigma-Aldrich) monomers were used. Monomers were dissolved in anhydrous toluene: acetonitrile (1:1 v/v) (0.1 M) immediately prior to use. Capping and oxidation reagents were identical to those used in DNA synthesis while ethylthiotetrazole (ETT) (0.25 M in acetonitrile, Link Technologies) was used as a coupling reagent. The coupling time for all monomers during RNA synthesis was 3 min. Stepwise coupling efficiencies were determined by automated trityl cation conductivity monitoring and in all cases were >97%.

Selective β-cyanoethyl removal: RNA and DNA bearing the 5′-primary amines were treated on-column with diethylamine (20% in anhydrous acetonitrile) for 20 min at room temperature. The resin was then washed with acetonitrile (3 × 1 ml) and dried with argon.

DNA deprotection: DNA was cleaved from solid support and deprotected by exposure to a concentrated solution of aqueous ammonia in a sealed vial for 5 hours at 55°C. After drying in vacuo, oligonucleotides were dissolved in water and subject to further purification.

RNA deprotection (2'-O-TC): The solid support was exposed to dry ethylenediamine: toluene (1:1 v/v) for 6 hours at room temperature, washed with toluene (3 × 1 ml) then acetonitrile (3 × 1 ml), and dried using argon. The cleaved RNA was eluted with water and purified using RP-HPLC.

RP-HPLC purification: DNA and RNA and were purified using an Agilent system with Kinetex C18 column (10 mm by 250 mm, pore size 100 Å, particle size 5 μm), a gradient of buffer A (0.1 M TEAA, pH 7.5) to buffer B (0.1 M TEAA, pH 7.5 50% v/v acetonitrile), and flow rate of 5 ml/min. A gradient of 0 to 50% buffer B over 28 min at 55°C was used in all cases. After HPLC, Amicon Ultra-4 0.5-ml centrifugal filters (Merck, cat. no. UFC5x) were used to desalt and concentrate oligonucleotide samples.

Postsynthetic oligonucleotide modification: Freeze-dried oligonucleotide (20 nmol) was dissolved in $NaHCO_3$ buffer (0.5 M, pH 8.5, 30 μl) and mixed with ATTO NHS ester (200 nmol, 20 μl) dissolved in DMSO. The reaction was then left for 4 hours at 25°C with 750 rpm shaking. After dilution with water, the samples were desalted using NAP-10 Columns (Cytivia, cat. no. 17085402) according to the manufacturer's instructions. RNA or DNA oligonucleotides were purified using HPLC as described above.

Oligonucleotide mass spectrometry: All DNA and RNA were characterized by negative-mode electrospray using a UPLC-MS Waters XEVO G2-QTOF mass spectrometer and an Acquity UPLC system with a BEH C18 1.7-μm column (Waters). A gradient of methanol in triethylamine (TEA) and hexafluoroisopropanol (HFIP) was used [buffer A, 8.6 mM TEA, 200 mM HFIP in 5% methanol/water (v/v); buffer B, 20% v/v buffer A in methanol]. Buffer B was increased from 0 to 70% over 7.5 min or 15 to 30% over 12.5 min for normal oligonucleotides and 50 to 100% over 7.5 min for hydrophobic oligonucleotides. The flow rate was set to 0.2 ml/min. Raw data were processed and deconvoluted using the deconvolution software MassLynx v4.1 and Unidec (*65*); see fig. S4.

IR-ECD purification and labeling

The IR-ECD was purified as previously described by Gutmann *et al.* (*51*). For labeling fivefold molar excess of Alexa Fluor 532 NHS ester (A20001, Thermo Fisher Scientific) was used. The reaction was performed on ice for 1 hour and was quenched with a fivefold molar excess of buffered ethanolamine over Alexa Fluor 532 NHS. The labeled protein was separated from free dye on a Superdex 200 Increase 10/300 GL column equilibrated with 25 mM Hepes, 150 mM NaCl, pH 7.4. The protein was aliquoted and snap-frozen with liquid nitrogen.

ETs experimental procedure

Fluorescence microscopy: Microfluidic devices were fabricated using previously described procedures (*7*, *24*), with the exception that in this study, all silicon dioxide etches were performed using reactive ion etching, and the silicon and glass substrates were thermally rather than anodically bonded. 10 to 100 μl of sample is loaded into one pair of loading reservoirs, while the other pair of reservoirs are sealed and connected to a vacuum pump (fig. S5). The pressure drop across the length of the channels loads the molecules into the trapping area under steady Poiseuille flow. Movies of fluorescent molecules diffusing through the trapping nanostructures are recorded either with the pressure drop applied (under flow), or without, depending on the modality of experiment. Movies are recorded for 1 to 10 min using an epi-fluorescent widefield fluorescent microscope at a frame rate of 100 Hz, generally, with an exposure time of 5 ms. A detailed description of the setup can be found in previous work (*3*). Briefly, for the measurements reported in this study, a 3 W, 532-nm DPSS laser (Del Mar Photonics) is used to illuminate a ~150 μm by 150 μm region of the device through a water-immersion objective (UPlanSApo 60× W, 1.2 NA, Olympus). The emission is filtered with a 532-nm cut-off dichroic and long-pass filters (Chroma), and imaged on an sCMOS camera (Kinetix, Photometrix).

Data analysis to determine the escape time of a molecular species: Recorded movies of molecules in the trap landscape are analyzed as described in previous work (*3*). Durations of residence times, Δt, of molecules in traps are extracted from intensity versus time traces, recorded for each trap locus. At present, a 1-min movie typically yields ~10^4 escape events. The average escape time is the mean of the all the residence times collected, $t_{\mathrm{av}} = \frac{1}{N}\sum \Delta t$, for a total number of residence times, N. The uncertainty on determining t_{av} in such a measurement is given by the standard error of all recorded residence times, $t_{\mathrm{av,e}} \cong \frac{t_{\mathrm{av}}}{\sqrt{N}}$. When fits of the data are performed, a histogram of residence times is fitted with a decaying single exponential function, $P_{\mathrm{f}}(\Delta t)$ with $k = 1$ as shown in Eq. 2, e.g., to determine a fitted escape time, $t_{\mathrm{esc}} = t_i$. Here, k is the number of components, E_i is the amplitude of the component with escape timescale, t_i, and c is a constant value capturing an experimental offset.

$$P_{\mathrm{f}}(\Delta t) = \sum_{i=1}^{k}\left(\frac{E_i}{t_i}\mathrm{e}^{-\frac{\Delta t}{t_i}}\right) + c \qquad (2)$$

The fit error on t_{esc} captures the SEM and, in general, corresponds well to $t_{\mathrm{av,e}}$ as expected.

REFERENCES AND NOTES

1. J. Han, H. G. Craighead, Separation of long DNA molecules in a microfabricated entropic trap array. *Science* **288**, 1026–1029 (2000). doi: 10.1126/science.288.5468.1026; pmid: 10807568
2. E. C. Yusko *et al.*, Real-time shape approximation and fingerprinting of single proteins using a nanopore. *Nat. Nanotechnol.* **12**, 360–367 (2017). doi: 10.1038/nnano.2016.267; pmid: 27992411
3. F. Ruggeri *et al.*, Single-molecule electrometry. *Nat. Nanotechnol.* **12**, 488–495 (2017). doi: 10.1038/nnano.2017.26; pmid: 28288117
4. G. Young *et al.*, Quantitative mass imaging of single biological macromolecules. *Science* **360**, 423–427 (2018). doi: 10.1126/science.aar5839; pmid: 29700264
5. H. Wilson, Q. Wang, ABEL-FRET: Tether-free single-molecule FRET with hydrodynamic profiling. *Nat. Methods* **18**, 816–820 (2021). doi: 10.1038/s41592-021-01173-9; pmid: 34127856
6. S. Schmid, P. Stömmer, H. Dietz, C. Dekker, Nanopore electro-osmotic trap for the label-free study of single proteins and their conformations. *Nat. Nanotechnol.* **16**, 1244–1250 (2021). doi: 10.1038/s41565-021-00958-5; pmid: 34462599
7. B. Špačková *et al.*, Label-free nanofluidic scattering microscopy of size and mass of single diffusing molecules and nanoparticles. *Nat. Methods* **19**, 751–758 (2022). doi: 10.1038/s41592-022-01491-6; pmid: 35637303
8. R. P. B. Jacquat *et al.*, Single-Molecule Sizing through Nanocavity Confinement. *Nano Lett.* **23**, 1629–1636 (2023). doi: 10.1021/acs.nanolett.1c04830; pmid: 36826991
9. L.-M. Needham *et al.*, Label-free detection and profiling of individual solution-phase molecules. *Nature* **629**, 1062–1068 (2024). doi: 10.1038/s41586-024-07370-8; pmid: 38720082
10. S. Ohayon *et al.*, Full-Length Single Protein Molecules Tracking and Counting in Thin Silicon Channels. *Adv. Mater.* **36**, e2314319 (2024). doi: 10.1002/adma.202314319; pmid: 38461367
11. M. Friedel, A. Baumketner, J.-E. Shea, Effects of surface tethering on protein folding mechanisms. *Proc. Natl. Acad. Sci. U.S.A.* **103**, 8396–8401 (2006). doi: 10.1073/pnas.0601210103; pmid: 16709672
12. Y. Pang, R. Gordon, Optical trapping of a single protein. *Nano Lett.* **12**, 402–406 (2012). doi: 10.1021/nl203719v; pmid: 22171921
13. F. Perrin, Mouvement Brownien d'un ellipsoide (II). Rotation libre et dépolarisation des fluorescences. Translation et diffusion de molécules ellipsoidales. *J. Phys. Radium* **7**, 1–11 (1936). doi: 10.1051/jphysrad:01936007010100
14. A. Ortega, D. Amorós, J. García de la Torre, Prediction of hydrodynamic and other solution properties of rigid proteins from atomic- and residue-level models. *Biophys. J.* **101**, 892–898 (2011). doi: 10.1016/j.bpj.2011.06.046; pmid: 21843480
15. P. J. Fleming, K. G. Fleming, HullRad: Fast Calculations of Folded and Disordered Protein and Nucleic Acid Hydrodynamic Properties. *Biophys. J.* **114**, 856–869 (2018). doi: 10.1016/j.bpj.2018.01.002; pmid: 29490246
16. J. H. Krohn, A. Mamot, N. Kaletta, Y. Qutbuddin, P. Schwille, Fluorescence correlation spectroscopy for particle sizing: A notorious challenge. *Biophys. J.* 10.1016/j.bpj.2025.03.017 (2025). doi: 10.1016/j.bpj.2025.03.017; pmid: 40134216
17. A. G. Kikhney, D. I. Svergun, A practical guide to small angle X-ray scattering (SAXS) of flexible and intrinsically disordered proteins. *FEBS Lett.* **589** (19PartA), 2570–2577 (2015). doi: 10.1016/j.febslet.2015.08.027; pmid: 26320411
18. M. Bespalova, A. Behjatian, N. Karedla, R. Walker-Gibbons, M. Krishnan, Opto-Electrostatic Determination of Nucleic Acid Double-Helix Dimensions and the Structure of the Molecule-Solvent Interface. *Macromolecules* **55**, 6200–6210 (2022). doi: 10.1021/acs.macromol.2c00657; pmid: 35910310
19. R. Walker-Gibbons, X. Zhu, A. Behjatian, T. J. D. Bennett, M. Krishnan, Sensing the structural and conformational properties of single-stranded nucleic acids using electrometry and molecular simulations. *Sci. Rep.* **14**, 20582 (2024). doi: 10.1038/s41598-024-70641-x; pmid: 39232063
20. C. B. Müller *et al.*, Precise measurement of diffusion by multi-color dual-focus fluorescence correlation spectroscopy. *Europhys. Lett.* **83**, 46001 (2008). doi: 10.1209/0295-5075/83/46001
21. G. Krainer *et al.*, Single-molecule digital sizing of proteins in solution. *Nat. Commun.* **15**, 7740 (2024). doi: 10.1038/s41467-024-50825-9; pmid: 39231922

22. F. Ruggeri, M. Krishnan, Entropic Trapping of a Singly Charged Molecule in Solution. *Nano Lett.* **18**, 3773–3779 (2018). doi: 10.1021/acs.nanolett.8b01011; pmid: 29688720
23. G. Kloes *et al.*, Far-Field Electrostatic Signatures of Macromolecular 3D Conformation. *Nano Lett.* **22**, 7834–7840 (2022). doi: 10.1021/acs.nanolett.2c02485; pmid: 36125326
24. M. Krishnan, N. Mojarad, P. Kukura, V. Sandoghdar, Geometry-induced electrostatic trapping of nanometric objects in a fluid. *Nature* **467**, 692–695 (2010). doi: 10.1038/nature09404; pmid: 20930840
25. P. J. Flory, *Principles of Polymer Chemistry* (Cornell Univ. Press, 1953).
26. D. K. Wilkins *et al.*, Hydrodynamic radii of native and denatured proteins measured by pulse field gradient NMR techniques. *Biochemistry* **38**, 16424–16431 (1999). doi: 10.1021/bi991765q; pmid: 10600103
27. J. E. Kohn *et al.*, Random-coil behavior and the dimensions of chemically unfolded proteins. *Proc. Natl. Acad. Sci. U.S.A.* **101**, 12491–12496 (2004). doi: 10.1073/pnas.0403643101; pmid: 15314214
28. Y. Nojima, K. Iguchi, Y. Suzuki, A. Sato, The pH-dependent formation of PEGylated bovine lactoferrin by branched polyethylene glycol (PEG)-N-hydroxysuccinimide (NHS) active esters. *Biol. Pharm. Bull.* **32**, 523–526 (2009). doi: 10.1248/bpb.32.523; pmid: 19252310
29. F. Ruggeri, M. Krishnan, Lattice diffusion of a single molecule in solution. *Phys. Rev. E* **96**, 062406 (2017). doi: 10.1103/PhysRevE.96.062406; pmid: 29347432
30. R. E. Dickerson *et al.*, The anatomy of A-, B-, and Z-DNA. *Science* **216**, 475–485 (1982). doi: 10.1126/science.7071593; pmid: 7071593
31. R. P. Goodman *et al.*, Rapid chiral assembly of rigid DNA building blocks for molecular nanofabrication. *Science* **310**, 1661–1665 (2005). doi: 10.1126/science.1120367; pmid: 16339440
32. S. Fischer *et al.*, Shape and Interhelical Spacing of DNA Origami Nanostructures Studied by Small-Angle X-ray Scattering. *Nano Lett.* **16**, 4282–4287 (2016). doi: 10.1021/acs.nanolett.6b01335; pmid: 27184452
33. E. Poppleton, R. Romero, A. Mallya, L. Rovigatti, P. Šulc, OxDNA.org: A public webserver for coarse-grained simulations of DNA and RNA nanostructures. *Nucleic Acids Res.* **49**, W491–W498 (2021). doi: 10.1093/nar/gkab324; pmid: 34009383
34. A. A. Istratov, O. F. Vyvenko, Exponential analysis in physical phenomena. *Rev. Sci. Instrum.* **70**, 1233–1257 (1999). doi: 10.1063/1.1149581
35. Q. Wei *et al.*, Fluorescent imaging of single nanoparticles and viruses on a smart phone. *ACS Nano* **7**, 9147–9155 (2013). doi: 10.1021/nn4037706; pmid: 24016065
36. R. J. L. Townshend *et al.*, Geometric deep learning of RNA structure. *Science* **373**, 1047–1051 (2021). doi: 10.1126/science.abe5650; pmid: 34446608
37. K. Zhang *et al.*, Cryo-EM structure of a 40 kDa SAM-IV riboswitch RNA at 3.7 Å resolution. *Nat. Commun.* **10**, 5511 (2019). doi: 10.1038/s41467-019-13494-7; pmid: 31796736
38. A. D. Garst, A. Héroux, R. P. Rambo, R. T. Batey, Crystal structure of the lysine riboswitch regulatory mRNA element. *J. Biol. Chem.* **283**, 22347–22351 (2008). doi: 10.1074/jbc.C800120200; pmid: 18593706
39. C. D. Stoddard *et al.*, Free state conformational sampling of the SAM-I riboswitch aptamer domain. *Structure* **18**, 787–797 (2010). doi: 10.1016/j.str.2010.04.006; pmid: 20637415
40. W. Palau, C. Di Primo, Single-cycle kinetic analysis of ternary DNA complexes by surface plasmon resonance on a decaying surface. *Biochimie* **94**, 1891–1899 (2012). doi: 10.1016/j.biochi.2012.04.025; pmid: 22580385
41. I. Jarmoskaite, I. AlSadhan, P. P. Vaidyanathan, D. Herschlag, How to measure and evaluate binding affinities. *eLife* **9**, e57264 (2020). doi: 10.7554/eLife.57264; pmid: 32758356
42. J. SantaLucia Jr., D. Hicks, The thermodynamics of DNA structural motifs. *Annu. Rev. Biophys. Biomol. Struct.* **33**, 415–440 (2004). doi: 10.1146/annurev.biophys.32.110601.141800; pmid: 15139820
43. H. Wilson, M. Lee, Q. Wang, Probing DNA-protein interactions using single-molecule diffusivity contrast. *Biophys. Rep.* **1**, 100009 (2021). doi: 10.1016/j.bpr.2021.100009; pmid: 36425309
44. C. J. Barnstable *et al.*, Production of monoclonal antibodies to group A erythrocytes, HLA and other human cell surface antigens-new tools for genetic analysis. *Cell* **14**, 9–20 (1978). doi: 10.1016/0092-8674(78)90296-9; pmid: 667938
45. M. N. Hug *et al.*, HLA antibody affinity determination: From HLA-specific monoclonal antibodies to donor HLA specific antibodies (DSA) in patient serum. *HLA* **102**, 278–300 (2023). doi: 10.1111/tan.15047; pmid: 37191252
46. M. M. Schneider *et al.*, Microfluidic antibody affinity profiling of alloantibody-HLA interactions in human serum. *Biosens. Bioelectron.* **228**, 115196 (2023). doi: 10.1016/j.bios.2023.115196; pmid: 36921387
47. W. Yoshida *et al.*, Selection of DNA aptamers against insulin and construction of an aptameric enzyme subunit for insulin sensing. *Biosens. Bioelectron.* **24**, 1116–1120 (2009). doi: 10.1016/j.bios.2008.06.016; pmid: 18644711
48. Z. Hao *et al.*, Real-Time Monitoring of Insulin Using a Graphene Field-Effect Transistor Aptameric Nanosensor. *ACS Appl. Mater. Interfaces* **9**, 27504–27511 (2017). doi: 10.1021/acsami.7b07684; pmid: 28770993
49. D. Wu *et al.*, Flow-Cell-Based Technology for Massively Parallel Characterization of Base-Modified DNA Aptamers. *Anal. Chem.* **95**, 2645–2652 (2023). doi: 10.1021/acs.analchem.1c04777; pmid: 36693249
50. J. G. Menting *et al.*, How insulin engages its primary binding site on the insulin receptor. *Nature* **493**, 241–245 (2013). doi: 10.1038/nature11781; pmid: 23302862
51. T. Gutmann *et al.*, Cryo-EM structure of the complete and ligand-saturated insulin receptor ectodomain. *J. Cell Biol.* **219**, e201907210 (2020). doi: 10.1083/jcb.201907210; pmid: 31727777
52. P. De Meyts, J. Whittaker, Structural biology of insulin and IGF1 receptors: Implications for drug design. *Nat. Rev. Drug Discov.* **1**, 769–783 (2002). doi: 10.1038/nrd917; pmid: 12360255
53. V. V. Kiselyov, S. Versteyhe, L. Gauguin, P. De Meyts, Harmonic oscillator model of the insulin and IGF1 receptors' allosteric binding and activation. *Mol. Syst. Biol.* **5**, 243 (2009). doi: 10.1038/msb.2008.78; pmid: 19225456
54. T. Gutmann, K. H. Kim, M. Grzybek, T. Walz, Ü. Coskun, Visualization of ligand-induced transmembrane signaling in the full-length human insulin receptor. *J. Cell Biol.* **217**, 1643–1649 (2018). doi: 10.1083/jcb.201711047; pmid: 29453311
55. T. I. Croll *et al.*, Higher-Resolution Structure of the Human Insulin Receptor Ectodomain: Multi-Modal Inclusion of the Insert Domain. *Structure* **24**, 469–476 (2016). doi: 10.1016/j.str.2015.12.014; pmid: 26853939
56. X. Xiong *et al.*, Symmetric and asymmetric receptor conformation continuum induced by a new insulin. *Nat. Chem. Biol.* **18**, 511–519 (2022). doi: 10.1038/s41589-022-00981-0; pmid: 35289328
57. P. A. Hoyne *et al.*, High affinity insulin binding by soluble insulin receptor extracellular domain fused to a leucine zipper. *FEBS Lett.* **479**, 15–18 (2000). doi: 10.1016/S0014-5793(00)01872-X; pmid: 10940380
58. F. Weis *et al.*, The signalling conformation of the insulin receptor ectodomain. *Nat. Commun.* **9**, 4420 (2018). doi: 10.1038/s41467-018-06826-6; pmid: 30356040
59. F. Kilár, I. Simon, The effect of iron binding on the conformation of transferrin. A small angle x-ray scattering study. *Biophys. J.* **48**, 799–802 (1985). doi: 10.1016/S0006-3495(85)83838-8; pmid: 4074838
60. H. Hwang, S. Myong, Protein induced fluorescence enhancement (PIFE) for probing protein-nucleic acid interactions. *Chem. Soc. Rev.* **43**, 1221–1229 (2014). doi: 10.1039/C3CS60201J; pmid: 24056732
61. F. Ruggeri, M. Krishnan, Spectrally resolved single-molecule electrometry. *J. Chem. Phys.* **148**, 123307 (2018). doi: 10.1063/1.5008936; pmid: 29604878
62. A. Langer *et al.*, A New Spectral Shift-Based Method to Characterize Molecular Interactions. *Assay Drug Dev. Technol.* **20**, 83–94 (2022). doi: 10.1089/adt.2021.133; pmid: 35171002
63. F. L. Sendker *et al.*, Emergence of fractal geometries in the evolution of a metabolic enzyme. *Nature* **628**, 894–900 (2024). doi: 10.1038/s41586-024-07287-2; pmid: 38600380
64. A. Aguzzi, T. O'Connor, Protein aggregation diseases: Pathogenicity and therapeutic perspectives. *Nat. Rev. Drug Discov.* **9**, 237–248 (2010). doi: 10.1038/nrd3050; pmid: 20190788
65. M. T. Marty *et al.*, Bayesian deconvolution of mass and ion mobility spectra: From binary interactions to polydisperse ensembles. *Anal. Chem.* **87**, 4370–4376 (2015). doi: 10.1021/acs.analchem.5b00140; pmid: 25799115
66. S. G. Schultz, A. K. Solomon, Determination of the effective hydrodynamic radii of small molecules by viscometry. *J. Gen. Physiol.* **44**, 1189–1199 (1961). doi: 10.1085/jgp.44.6.1189; pmid: 13748878

ACKNOWLEDGMENTS

We gratefully acknowledge A. Turberfield for the kind gift of DNA nanostructures, the NIH Tetramer Core Facility (contract no.75N93020D00005) for providing HLA-A*03:01, and Robin W. Klemm for helpful discussions. **Funding:** This research was supported by European Research Council Consolidator Grant 724180 (X.Z., T.J.D.B., M.K.), Biotechnology and Biological Sciences Research Council BB/W017415/1 (D.S., X.Z., M.K.), the Wellcome LEAP Delta Tissue Program (X.Z., K.C.Z., J.L.P.B., M.K.), Royal Society Research Grant RGS\R2\242523 (A.H.E.-S.), Royal Society of Chemistry Research grant R24-8767374007 (A.H.E.-S.), the Federal Ministry of Education and Research (BMBF), and the German Center for Diabetes Research (DZD e.V.) (U.C.). **Author contributions:** Conceptualization and model: M.K.; Data analysis and processing: T.J.D.B.; Measurement: X.Z., T.J.D.B., D.S.; Methodology: X.Z., T.J.D.B., M.K.; Nucleic acid design, synthesis, and quality control: A.H.E.-S.; Protein synthesis/recombinant production, labeling, and quality control: K.C.Z., M.G., J.L.P.B., U.C.; Supervision: M.K.; Visualization: T.J.D.B., X.Z., K.C.Z., D.S., M.K.; Writing – original draft: M.K.; Writing – review & editing: All authors. **Competing interests:** Novel aspects described in this work are covered by a patent application filed by M.K. to which X.Z., T.J.D.B., K.C.Z., and D.S. have contributed. M.K. is also founding a company aiming to commercialize aspects of this work. **Data and materials availability:** All data are available in the main text or the supplementary materials.

SUPPLEMENTARY MATERIALS

science.org/doi/10.1126/science.adt5827
Supplementary Text; Figs. S1 to S24; Tables S1 to S5; References (*67*–*85*); Movies S1 and S2; MDAR Reproducibility Checklist

Submitted 7 October 2024; accepted 14 March 2025

10.1126/science.adt5827